

Article

Study of the Effects of Hardfacing Modes Carried out by FCAW-S with Exothermic Addition of MnO₂-Al on Non-Metallic Inclusions, Grain Size, Microstructure and Mechanical Properties

Bohdan Trembach^{1,*}, Illia Trembach², Aleksandr Grin², Nataliia Makarenko², Olha Babych³,
Sergey Knyazev⁴, Yuliia Musairova³, Michal Krbata⁵, Oleksii Balenko⁶, Oleh Vorobiov³ and
Anatoliy Panchenko³

¹ Rappresentanze Industriali M&C Division doo, 52000 Pazin, Croatia

² Welding Technology Department, Donbas State Engineering Academy, 84313 Kramatorsk, Ukraine; i_trembach@ukr.net (I.T.); aleksandrgrin54@gmail.com (A.G.); natal@mail.ru (N.M.)

³ Scientific Research Laboratory, Ivan Kozhedub Kharkiv National Air Force University, 61045 Kharkiv, Ukraine; y.musairova@hnups.mil.gov.ua (Y.M.); o.vorobiov@hnups.mil.gov.ua (O.V.); martensid1929@gmail.com (A.P.)

⁴ Department of Materials Science, National Technical University "Kharkiv Polytechnic Institute", 61000 Kharkiv, Ukraine; obmeninfo@ukr.net

⁵ Faculty of Special Technology, Alexander Dubcek University of Trenčín, 911 06 Trenčín, Slovakia; michal.krbata@tnuni.sk

⁶ Department of Computer Engineering and Programming, National Technical University "Kharkiv Polytechnic Institute", 61000 Kharkiv, Ukraine; alexibalenko@gmail.com

* Correspondence: btrembach89@gmail.com; Tel.: +380-99-450-0811

Abstract: This paper investigates self-shielded flux-cored wires with an exothermic MnO₂-Al addition and the effect of hardfacing modes on the deposited alloy of the Fe-C-Mn system for the first time. Additionally, the paper proposes a new experimental research methodology using an orthogonal experimental design with nine experiments and three levels. At the first stage, it is proposed to use the Taguchi plan (L9) method to find the most significant variables. At the second stage, for the development of a mathematical model and optimization, a factorial design is recommended. The studied parameters of the hardfacing mode were travel speed (*TS*), set voltage on the power source (U_{set}), contact tip to work distance (*CTWD*), and wire feed speed (*WFS*). The following parameters were studied: welding thermal cycle parameters, microstructure, grain size, non-metallic inclusions, and mechanical properties. The results of the analysis showed that the listed parameters of the hardfacing modes have a different effect on the characteristics of the hardfacing process with self-shielded flux-cored wires with an exothermic addition in the filler. It was determined that for flux-cored wires with an exothermic addition, the size of the deposited metal grain size is most affected by the contact tip to work distance (*CTWD*). The research results showed that the travel speed (*TS*) had the main influence on the thermal cycle parameters (heat input, cooling time) and hardness. The analysis of the deposited metal samples showed that an increase in the travel speed had a negative impact on the number of non-metallic inclusions (NMIs) in the deposited metal. While the size of NMIs was influenced by the wire feed speed and the set voltage on the power source.

Keywords: Hadfield manganese steel; self-shielded flux-cored wire; exothermic addition; thermal cycle parameters; heat input; austenitic microstructure; grain size; hardness; non-metallic inclusions; Taguchi method; factorial design



Academic Editor: Tomasz Lipiński

Received: 30 April 2025

Revised: 31 May 2025

Accepted: 5 June 2025

Published: 10 June 2025

Citation: Trembach, B.; Trembach, I.; Grin, A.; Makarenko, N.; Babych, O.; Knyazev, S.; Musairova, Y.; Krbata, M.; Balenko, O.; Vorobiov, O.; et al. Study of the Effects of Hardfacing Modes Carried out by FCAW-S with Exothermic Addition of MnO₂-Al on Non-Metallic Inclusions, Grain Size, Microstructure and Mechanical Properties. *Eng* **2025**, *6*, 125. <https://doi.org/10.3390/eng6060125>

Copyright: © 2025 by the authors. Licensee MDPI, Basel, Switzerland. This article is an open access article distributed under the terms and conditions of the Creative Commons Attribution (CC BY) license (<https://creativecommons.org/licenses/by/4.0/>).

1. Introduction

Welding and hardfacing technologies can provide competitive advantages such as cost and quality of the final product in agriculture, mechanical engineering [1], the automotive industry [2,3], the transport sector [4,5], and other industries. In addition, the use of surfacing technology can extend the service life of worn surfaces subjected to various types of destruction (abrasive [6–13], corrosive [9], abrasive-impact [10,11], and others). In each of these sectors of the economy, the application of welding technologies and welding materials is essential. Among the variety of welding materials, the following are distinguished: stick electrodes, solid wires, flux-cored wires, and SAW wires and fluxes [12,13]. Recent publications have shown that flux-cored wire hardfacing is a promising technology [14,15], which is explained by its high process performance, high welding stability, excellent quality of deposited metal, and arc visibility. These advantages are especially important for hardfacing processes using hardening alloys. Depending on the tribological conditions, different alloys are used, such as Fe-C-Cr-X ($X = \text{Ti, Nb, V}$) [16,17], Fe-C-B [18,19], Fe-C-Mn [20], and others. High-manganese alloys of the Fe-C-Mn type with a high manganese and carbon content have been most widely used for impact abrasive wear and contact fatigue in high-stress rolling [21,22]. These steels are characterized by high impact strength and the ability to harden [23]. Hadfield steel has good work hardening capacity, high strength and toughness after hardening, and it has been widely used in industrial applications. However, the presence of non-metallic inclusions significantly affects its wear behavior. This study investigates the role of these inclusions in the abrasive wear process of Hadfield steel by examining their formation, distribution, and impact on mechanical properties. The results suggest that non-metallic inclusions act as stress concentrators, promoting crack initiation and propagation, thereby accelerating material removal under abrasive conditions. Thus, it is important to improve the quality of the deposited metal. The appearance of non-metallic inclusions in the deposited metal during the flux-cored wire hardfacing (FCAW-S) is mainly due to the melting nature of the flux-cored wire. Flux-cored wire consists of an inner flux and an outer metal sheath. According to Trembach et al. [24], the formation of the non-metallic inclusions (NMIs) occurs as follows: at the melting of the electrode, a protrusion of filler is formed at its end near the arc column. The formation of the protrusion is explained by the non-uniformity of the melting of the metal sheath and the filler in the flux-cored wire. That is explained by the predominant heating of the metal sheath by Joule heat (welding current flowing through the electrode) due to the significantly higher electrical conductivity of the metal sheath [24]. The second reason is the cathode spot relocations of the arc column around the perimeter of the end of the metal sheath [25]. In this case, the melting of the filler material from the arc heat is realized by radiation of the arc column and, to a lesser extent, by convective heat. These features contribute to the preferential melting of the metal sheath, which is the main reason for the uneven melting of the filler and the metal sheath. The formed protrusion can subsequently collapse and, in the unmelted state, enter the weld pool [24].

It is well known that there are three modes of transferring the metal droplet to the molten pool: spray, globular, and short circuit [26]. For hardfacing processes, when the chemical composition of the deposited metal is important, which is always more alloyed than substrate materials, the last two modes are preferable. In spray and globular modes of the molten droplet transfer, the arc continues burning throughout the molten droplet transfer process, providing high heat input, which increases the fraction of the substrate material. While in the short circuit transfer mode, the molten droplet transfer occurs when the droplet at the wire tip comes into contact with the weld pool under conditions of low current and voltage, causing the arc to be extinguished. This results in relatively low heat input [26], which is beneficial for hardfacing processes. When the welding arc between

the wire tip and the weld pool is extinguished, a short circuit occurs, which causes the arc voltage to drop below ~ 10 V, which can be used to evaluate the occurrence of a short-circuit procedure [27]. However, this reduces the deposition rate because it is achieved at lower values of the welding current.

To improve the uniformity of melting of the flux-cored wire and to increase the productivity of the hardfacing process, the introduction of exothermic addition into the filler for flux-cored wires is accepted [28–30]. The positive effect of introducing the exothermic addition into the filler is explained by the generation of additional heat capable of melting the filler components [31]. Various exothermic additive systems are used, which are different combinations of oxidizing agents (such as Fe_2O_3 , CuO , Mn_2O , etc.) and reducing agents (Al, Mg, etc.). However, these exothermic mixtures have different characteristics of reaction kinetics; among the important ones for filler materials are ignition temperature, reaction rate, thermal effect of the exothermic reaction, and specific heat of combustion.

The study by Li et al. [32] showed a positive effect of the exothermic mixture on the stability of the process; the droplets became smaller and the transfer time became less with increasing the exothermic addition. The decrease in the droplet diameter of the electrode material is mainly due to a decrease in surface tension [32]. Trembach et al. [33] noted that, depending on the hardfacing modes, the exothermic reaction in the filler can occur at different stages of the welding process: (1) in the electrode extension section, (2) in the arc column, and (3) in the weld pool. Moreover, from the point of view of achieving a greater effect from the introduction of an exothermic addition, the reaction at stage (1) is the most desirable. In accordance with their recommendations, it is necessary to choose such hardfacing parameters at which the exothermic mixture reacts at the electrode melting stage (in the electrode extension section) before the arc. At the same time, high arc stability and low dilution of the deposited metal with the substrate materials are achieved while maintaining high productivity and efficiency of the hardfacing process [33], whereas the exothermic reaction at the weld pool stage will increase the penetration depth and increase the dilution of the deposited metal by the substrate material [34], which is undesirable for the hardfacing process. Furthermore, studies by Trembach et al. have shown a positive effect of adding the exothermic addition to the filler on the welding current [33] and the morphology of the welding bead [35], which changes the parameters of the welding thermal cycle [36,37]. Changes in the welding thermal cycle parameters will affect the microstructure, which will affect the performance indicators such as wear resistance and corrosion resistance through the impact on the microstructure and mechanical properties.

The aim of this work is to determine the influence of hardfacing modes on such parameters as hardfacing thermal cycle parameters, microstructure, grain size, hardness, and content and morphology of non-metallic inclusions of the deposited metal using a self-shielded flux-cored wire with high-energy exothermic addition of $\text{MnO}_2\text{-Al}$.

2. Materials and Methods

2.1. Materials

For the hardfacing process, flux-cored wires with filler compositions as shown in Table 1 were used. A metal strip made of St 24 DIN 1614.1 [38] steel (20 mm in width and 0.5 mm in thickness) was used, which was formed into a metal wire sheath about the core filler. The self-shielded flux-cored wire was made according to the procedure described in [24].

The substrate material comprised plates with dimensions of $200 \times 100 \times 15$ mm (length \times width \times thickness). The material of the plates was S235 J2G2 EN 10025–2 (St3ps). The hardfacing was carried out with reverse polarity by an ABC automatic welding head. The power source of the machine had a rigid external characteristic.

Table 1. Composition of core filler FCAW-SS, wt.%.

The Name of the Component	Content of the Components in Core Filler of FCAW-S [wt.%]
Gas-slag-forming components	
Fluorite concentrate GOST 4421-73	10
Rutile concentrate GOST 22938-78	6
Calcium carbonate GOST 8252-79	3
Zirconium dioxide GOST 21907-76	3
Components of exothermic addition	
Oxide of manganese powder-like GOST 4470-79	21
Aluminum powder PA1 GOST 6058-73	9
Alloying and deoxidizers	
Ferromanganese FMN-88A GOST 4755-91	20
Ferrosilicon FS-92 GOST 1415-78	2
Titanium powder PTM-3 TU 14-22-57-92	5
Metal Chrome X99 GOST 5905-79	6.2
Oxide of yttrium powder-like TU 48-4-524-80	1.6
Graphite	7.6
Iron powder PZhR-1 GOST 9849-86	5.6

The hardfacing process was carried out in four layers. The height of the hardfacing layer was 5–7 mm. This depended on the hardfacing modes. The chemical composition of the deposited metal samples was analyzed using a Spectrolab LAVFC01A (Ametek, Inc., Berwyn, IL, USA) optical emission spectrometer. The typical content of the elements in the deposited metal is as follows: 1.36 wt% C; 9.3 wt% Mn; 2.8 wt% Cr; 0.76 wt% Ti; 0.72 wt% Si; 0.046 wt% N; 0.02 wt% S; and 0.058 wt% P.

2.2. Design of the Experiment

When searching for models of mathematical dependencies, the most important task is the choice of variables. Having too many variables (with respect to the number of observations/data sets) in a model will result in a relation between variables and the outcome that only exists in that particular data set [39]. Some variables also may have a negligible effect on the outcome and can therefore be excluded. In this case, a preliminary review of possible variables will be mandatory, which in the future, after screening, will be used to search for a mathematical model. Therefore, we recommend that at the first stage of searching for a prediction model, the most significant parameters from a series of candidate variables are determined. Taguchi is another method suitable to the optimization of welding processes that can be used in the design of high-quality systems without increasing costs, allowing for understanding the effect of individual and combined process parameters from reduced experimental tests. For the Taguchi method, orthogonal arrays were used. An analysis of variance (ANOVA) is used in parallel with the Taguchi method. Analysis of variance (ANOVA) allows us to determine the contribution of each factor to the responses, which allows us to identify the most significant variables [40]. Factorial design is used for conducting experiments as it allows the study of interactions between factors. Reliable mathematical models of the variables of interest can be developed with a minimum number of experiments by combining the Taguchi method with factorial design. [41].

The Taguchi method was then used to obtain the welding combinations that are shown in Table 2. The variable parameters of the hardfacing modes, i.e., hardfacing speed (x1), set voltage of the power source (x2), contact tip to work distance (x3), and wire feed speed (x4), were optimized using the Box–Behnken experimental design and STATISTICA software Version 6.0 (Statsoft Inc., Hamburg, Germany, 2006). The experimental design contained four process variables, each at three equidistant levels (1, 2, 3).

Table 2. Input variables selected and their levels.

Code	Input Variable (Factor)	Unit	Notation	Level		
				Low (1)	Average (2)	High (3)
A	Travel speed	[m·min ⁻¹]	<i>TS</i>	0.27	0.47	0.69
B	Arc welding voltage	[V]	<i>U_{set}</i>	26.0	29.2	32.5
C	Contact tip to work distance	[mm]	<i>CTWD</i>	30	40	50
D	Wire feed speed	[m·min ⁻¹]	<i>WFS</i>	1.50	2.07	2.73

The matrix of the experimental plan is shown in Table 3. The three different processing variables combined with each of the three levels led to an L9 orthogonal matrix.

Table 3. Design matrix of the experimental full factor analysis using the orthogonal array from the method.

№	Code Mean				Fact Mean			
	Factor A	Factor B	Factor C	Factor D	<i>TS</i> [m·min ⁻¹]	<i>U_{set}</i> [V]	<i>CTWD</i> [mm]	<i>WFS</i> [m·min ⁻¹]
1	1	1	1	1	0.27	26.0	30	1.50
2	1	2	2	2	0.27	29.2	40	2.07
3	1	3	3	3	0.27	32.5	50	2.73
4	2	1	2	3	0.47	26.0	40	2.73
5	2	2	3	1	0.47	29.2	50	1.50
6	2	3	1	2	0.47	32.5	30	2.07
7	3	1	3	2	0.69	26.0	50	2.07
8	3	2	1	3	0.69	29.2	30	2.73
9	3	3	2	1	0.69	32.5	40	1.50

The full cubic model is represented in Equation (8):

$$y = \sum_{i=1}^K \beta_i \cdot x_i + \sum_{\substack{j>i \\ j=1}}^k \beta_{ij} \cdot x_i \cdot x_j + \sum_{\substack{j>i \\ j=1}}^k \delta_{ij} \cdot x_i \cdot x_j \cdot (x_i - x_j) + \sum_{\substack{k>j>i \\ k=1}}^K \beta_{ijk} \cdot x_i \cdot x_j \cdot x_k + \varepsilon \quad (1)$$

where *y* is the predicted response variable; *i* and *j* are the number of ingredients in the mixture; *K* are components given by the equation; β_i is the expected response at the top; β_{ij} are coefficients indicating the amount of quadratic curvature along the edge of the simplex region consisting of binary mixtures of *x_i* and *x_j*; and Δ_{ij} accounts for ternary blending among three separate components in the interior of the design. β_{ijk} is the coefficient of the regression coefficient of the product terms of two or three variables. *x_i*, *x_j*, and *x_k* represent three different design variables.

2.3. Welding Thermal Cycle Parameters

During the hardfacing process, the deposited metal experiences metallurgical effects caused by the thermal cycle of welding. To evaluate this effect, such indicators as heat input (*HI*), cooling rate (*CR₈₀₀₋₅₀₀*), and cooling time ($\Delta t_{8/5}$).

Heat input (*HI*) is the quantity of energy introduced from the arc per unit length of weld. The heat input was calculated by means of Equation (2) [36]:

$$HI = \frac{\eta_{FCAW} \cdot U_a \cdot I \cdot 60}{TS \cdot 1000} \quad (2)$$

where *HI* is the heat input, [kJ/mm]; *U_a* is arc voltage, V; *I* is arc current, A; *TS* is travel speed, mm/min; η_{FCAW} is the coefficient of efficiency of the process; and $\eta_{FCAW} = 0.8$.

The cooling rate (CR) has been calculated between 800 °C and 500 °C (CR800-500), as this temperature range is significant for the relevant phase transformations that take place in ferrous alloys and can be calculated using the following equation [36]:

$$CR_{800-500} = \frac{\Delta T_{800-500}}{\Delta t_{800-500}} \tag{3}$$

where $\Delta T_{800-500}$ is the temperature variation within the selected range of 800 and 500 °C.

The cooling time $\Delta t_{800-500}$ between two given temperatures, commonly between 800 and 500 °C, for sheets with three-dimensional heat flow, can be calculated by the following Equation (4) [36]:

$$\Delta t_{800-500} = \frac{E \cdot k}{2 \cdot \pi \cdot \lambda} \cdot \left[\frac{1}{500 - T_0} - \frac{1}{800 - T_0} \right] \tag{4}$$

where E is welding energy [$\text{kJ} \cdot \text{cm}^{-1}$], k is material thermal conductivity [$\text{J}/(\text{s} \cdot \text{m} \cdot \text{C})$] [36], and T_0 is the initial temperature of the plate $T_0 = 25$ °C.

3. Results

3.1. Prediction of Mathematical Model for Thermal Cycle Parameters

Table 4 shows the experimental and calculated (obtained from the equations of the mathematical model) values of the thermal cycle of hardfacing HI , cooling time in the temperature range of 800–500 °C ($\Delta t_{8/5}$), cooling rate (CR) of the deposited metal in the temperature range of 800–500 °C, and the calculated value of hardness (HB) obtained by hardfacing with the developed SFCW with exothermic addition (EA) of $\text{MnO}_2\text{-Al}$ in the filler material.

Table 4. Experimental and calculated values of thermal cycle parameters.

№	Average Welding Current I_{aw} [A]	Average Arc Voltage U_{aw} [V]	Heat Input			
			HI (e) [$\text{kJ} \cdot \text{mm}^{-1}$]	HI (c) [$\text{kJ} \cdot \text{mm}^{-1}$]	Diff. [$\text{kJ} \cdot \text{mm}^{-1}$]	Dev. [%]
1	240.4	22.30	0.905	0.894708	0.009947	1.14%
2	302.6	21.20	1.083	1.169728	−0.087176	−8.01%
3	358.5	25.30	1.531	1.453342	0.077229	5.07%
4	47.8	16.00	0.675	0.549353	0.126109	18.61%
5	213.6	28.00	0.577	0.697459	−0.120739	−20.88%
6	322.1	27.20	0.845	0.850193	−0.005370	−0.61%
7	325.0	19.60	0.414	0.481392	−0.066958	−16.28%
8	393.8	21.80	0.559	0.486719	0.071813	12.93%
9	259.2	28.90	0.487	0.492213	−0.004855	−1.07%

№	Cooling time				Cooling rate			
	$\Delta t_{8/5}$ (e) [s]	$\Delta t_{8/5}$ (c) [s]	Diff. [s]	Dev. [%]	CR (e) [$^{\circ}\text{C} \cdot \text{s}^{-1}$]	CR (c) [$^{\circ}\text{C} \cdot \text{s}^{-1}$]	Diff. [$^{\circ}\text{C} \cdot \text{s}^{-1}$]	Dev. [%]
1	4.207	4.160439	0.046254	1.11%	71.3	71.2216	0.0934	0.11%
2	5.034	5.439294	−0.405374	−8.05%	59.6	56.2343	3.3614	5.65%
3	7.117	6.758112	0.359120	5.04%	42.2	45.2460	−3.0948	−7.22%
4	3.141	2.554521	0.586415	18.67%	95.5	108.9094	−13.3965	−14.04%
5	2.682	3.243220	−0.561442	−20.93%	111.9	92.1757	19.6905	17.63%
6	3.928	3.953440	−0.024973	−0.65%	76.4	83.3396	−6.9739	−9.08%
7	1.927	2.238496	−0.311359	−16.16%	155.7	146.6686	9.0026	5.80%
8	2.597	2.263269	0.333932	12.85%	115.5	130.0900	−14.5811	−12.63%
9	2.266	2.288815	−0.022574	−1.01%	132.4	126.4793	5.8984	4.47%

The indices on the right side of the geometric parameter notation have the following meanings: (e)—experimental values; (c)—calculated values obtained by introducing the corresponding values of variables into the developed mathematical models.

3.1.1. Analyses of Variance for Thermal Cycle Parameters

Figure 1 shows the effect of the parameters of the hardfacing modes on the heat input (HI), cooling time in the temperature range of 800–500 °C $\Delta t_{8/5}$, and cooling rate (CR) of the deposited metal in the temperature range of 800–500 °C.

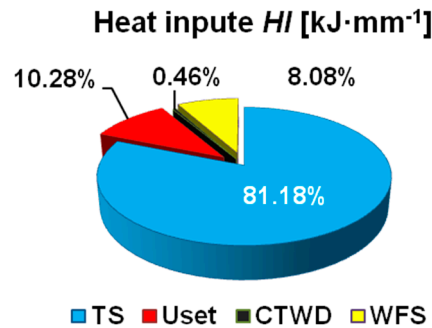


Figure 1. Pie chart of the influence of hardfacing mode parameters on the characteristics of the hardfacing thermal cycle.

Based on the above pie chart, it could be concluded that the main contribution to the parameters of the welding thermal cycle was made by the travel speed (TS). A minor influence was exerted by the set voltage of the power source. The influence of other parameters of the hardfacing modes on the welding thermal cycle parameters was at the level of noise.

3.1.2. Taguchi Analyses for Thermal Cycle Parameters

For the preliminary optimization of hardfacing modes, we conducted several studies, and Figure 2 shows the experimental results of the calculated S/N ratios for the heat input using the Taguchi method.

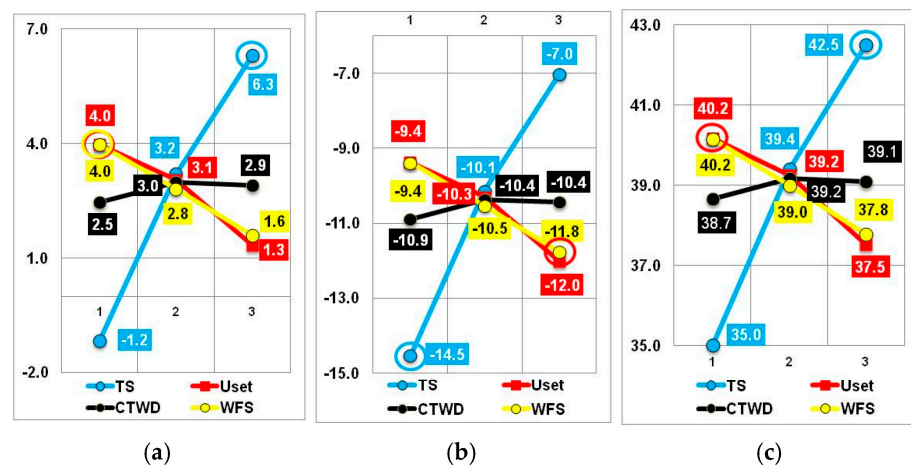


Figure 2. Diagram of the main effects of the S/N ratio for the characteristics of the hardfacing thermal cycle: (a) heat input (HI); (b) cooling time ($\Delta t_{8/5}$); (c) cooling rate (CR).

Figure 2a showed that the lowest value of heat input (HI) and cooling time $\Delta t_{8/5}$ in the temperature range of 800–500 °C was achieved at a low level of travel speed, $TS = 0.27 \text{ m}\cdot\text{min}^{-1}$. The lower the value of heat input (HI) and the cooling time in the temperature range of 800–500 °C $\Delta t_{8/5}$, the lower the level of overheating and, accordingly, the higher the technological properties of the deposited metal. Therefore, when selecting the optimal hardfacing parameters, it is of particular importance to ensure a low heat input and a high cooling rate in the temperature range of 800–500 °C $\Delta t_{8/5}$.

Analyzing the diagrams of S/N ratios for the thermal cycle parameters of hardfacing heat input and the cooling time in the temperature range of 800–500 °C $\Delta t_{8/5}$ (Figure 2a,b), the optimal hardfacing modes could be noted: travel speed, $TS = 0.27 \text{ m}\cdot\text{min}^{-1}$; set voltage on the power source, $U_{set} = 32.5 \text{ V}$; contact tip to work distance, $CTWD = 30 \text{ mm}$; and $WFS = 1.527 \text{ mm}\cdot\text{min}^{-1}$.

3.1.3. Development of a Mathematical Model (Box–Hunter) for Thermal Cycle Parameters

The equations for the mathematical dependence of the indicators are shown below (Equations (5)–(7)).

$$Y(HI) = 0.78 - 0.687 \cdot TS - 0.151 \cdot TS^2 + 0.285 \cdot U_{set} - 0.274 \cdot TS \cdot U_{set}. \tag{5}$$

$$Y(\Delta t_{8/5}) = 3.628 - 3.196 \cdot TS - 0.701 \cdot TS^2 + 1.324 \cdot U_{set} - 1.274 \cdot TS \cdot U_{set}. \tag{6}$$

$$Y(CR) = 96.288 + 76.818 \cdot TS - 23.807 \cdot U_{set} + 2.935 \cdot TS \cdot U_{set} - 15.655 \cdot TS \cdot U_{set}^2 + 3.612 \cdot TS^2 \cdot U_{set} + 18.943 \cdot TS^2 \cdot U_{set}^2. \tag{7}$$

Table 5 presents the regression coefficients for each response.

Table 5. Result of analysis of variance for the applied models on thermal cycle parameters.

Parameter	Coefficient of Determination R-Sqr	Adjusted Sum of Squares (SS)	Model Quality	MS Residual
Heat input (HI)	0.94589	0.89177	Good	0.0134593
Cooling rate (CR)	0.99986	0.99946	Very good	0.7312838
Cooling time ($\Delta t_{8/5}$)	0.94589	0.89177	Good	0.2910308

The statistical characteristics of the obtained mathematical models indicate their good quality.

The statistical significance and degree of influence of each of the factors on the dependent variables are represented by Pareto charts in Figure 3a–c, and graphs of the observed and predicted values of the influence of each factor on the dependent variables to assess the quality of the constructed mathematical models are shown in Figure 4a–c, respectively.

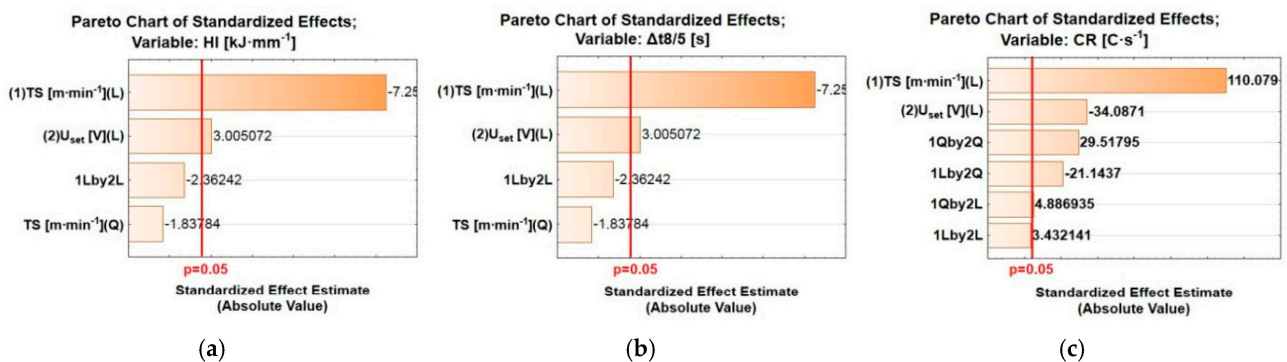


Figure 3. Pareto charts for the characteristics of the hardfacing thermal cycle: (a) heat input (HI); (b) cooling time ($\Delta t_{8/5}$); (c) cooling rate (CR).

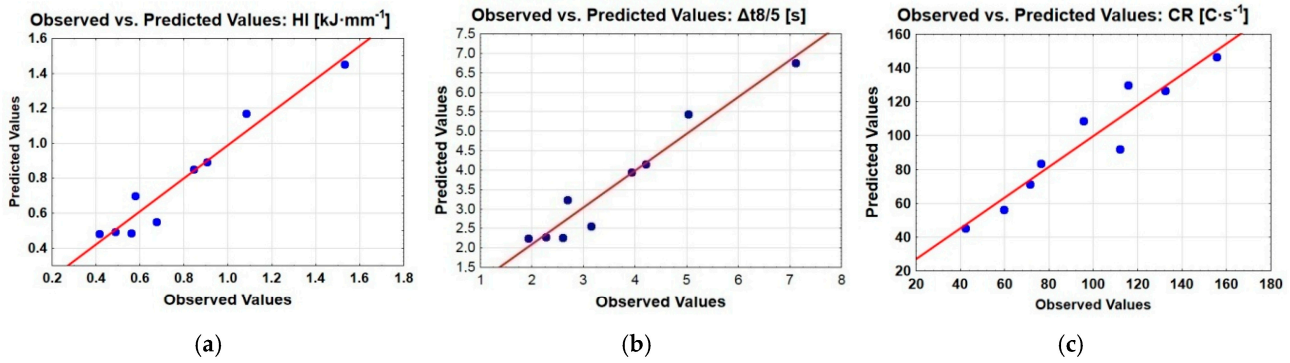


Figure 4. Graphs of the predicted values of the influence of each factor on the dependent variables for: (a) heat input (*HI*); (b) cooling time ($\Delta t_{8/5}$); (c) cooling rate (*CR*).

The analysis of the Pareto charts showed that the two terms of the mathematical model equation (*TS* and *U_{set}*) had the greatest impact on all indicators of the hardfacing thermal cycle. At the same time, the main factor was the travel speed. Analysis of Figure 4a–c showed a fairly high accuracy of the predicted values for all the constructed mathematical models.

Figure 5 shows the response surfaces of the mathematical model of the dependence of the hardfacing thermal cycle parameters on the parameters of the hardfacing modes.

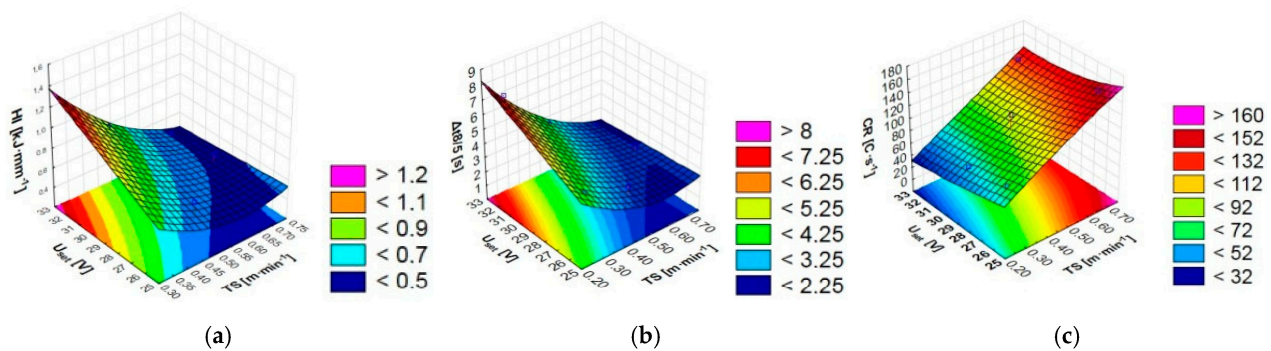


Figure 5. Response surfaces of the mathematical model of the dependence of hardfacing thermal cycle parameters: (a) heat input (*HI*); (b) cooling time ($\Delta t_{8/5}$); (c) cooling rate (*CR*).

The analysis of Figure 5 shows the dependence of the hardfacing thermal cycle parameters on the travel speed (*TS*) and, to a lesser extent, the set voltage on the power source (*U_{set}*), which affected the cooling rate of the deposited metal. If the heat input (*HI*) and the cooling rate in the temperature range of 800–500 °C $\Delta t_{8/5}$ reached their lowest values at a high level of *TS* = 0.69 m·min⁻¹, and regardless of the *U_{set}* level, the cooling rate (*CR*) increased with the increase in the level of travel speed (*TS*).

3.2. Microstructure of the Deposited Metal

Figure 6 shows the microstructures of the deposited metal using FCAW-S with EA in the filler, obtained by hardfacing at the conditions specified in Table 3.

Figure 6a shows a microstructure with pronounced traces of primary crystallization, represented by alloy-depleted austenite and highly dispersed precipitates of a secondary phase, first of all, in the form of titanium nitrides (TiN). A similar structure is shown in Figure 6b,c. However, in these cases, a deeper transformation of the dendrites was observed with a corresponding decrease in the boundary development and an increase in equilibrium from the thermodynamic point of view.

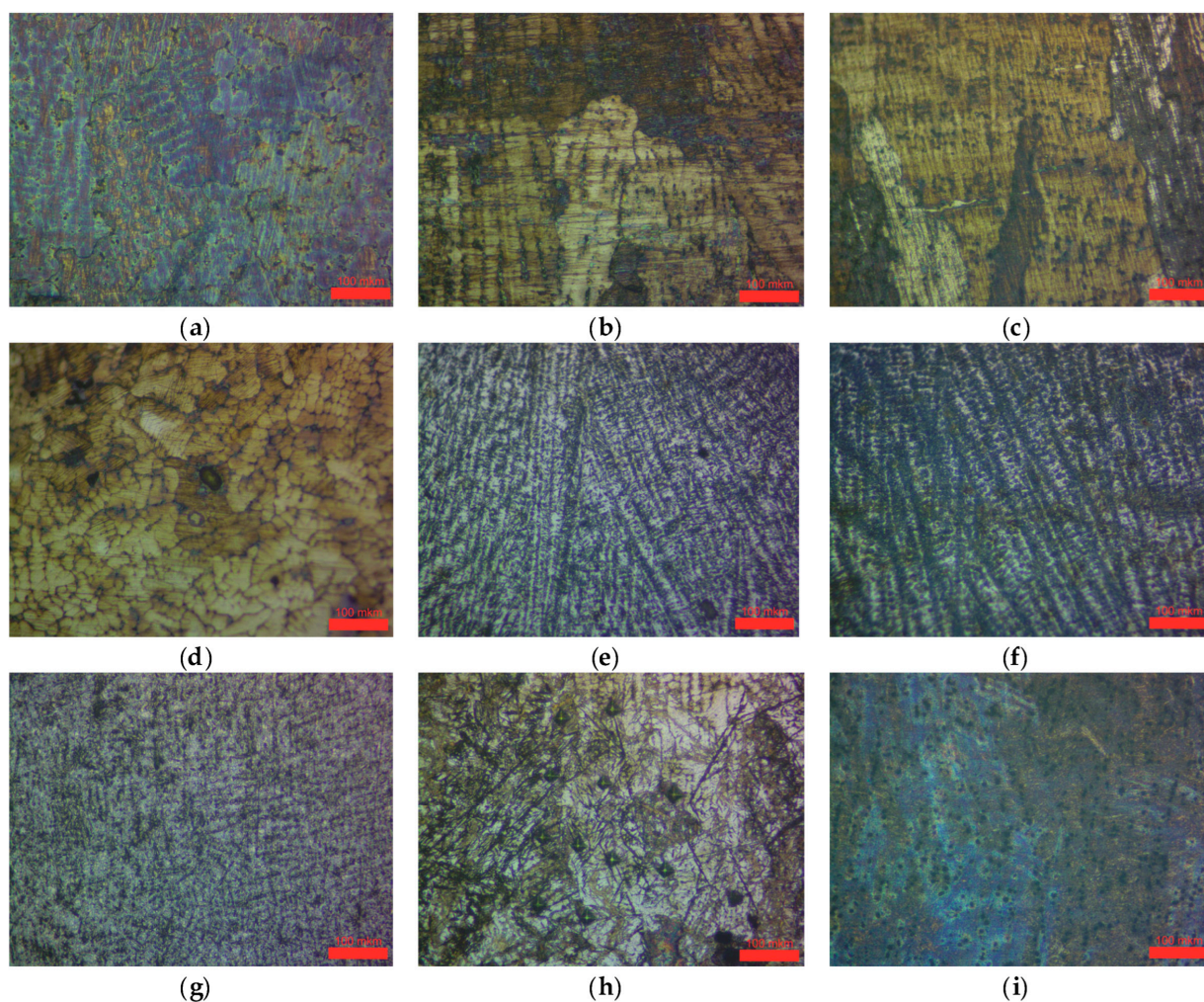


Figure 6. Microstructure of the deposited metal, $\times 200$: (a) Exp. 1, (b) Exp. 2, (c) Exp. 3, (d) Exp. 4, (e) Exp. 5, (f) Exp. 6, (g) Exp. 7, (h) Exp. 8, (i) Exp. 9.

A significant change in morphology was observed in the structure of sample Exp. 4 (Figure 6d). The dendritic structure could be traced, but it was highly fragmented. The matrix was an austenite saturated with alloying elements with very dispersed precipitates at the crystallite boundaries (degenerate interdendritic space) where the residual alloying elements and impurities were segregated.

The microstructure of Figure 6e is an acicular troostite and austenite with higher mechanical characteristics than the previous ones. The microstructure of Figure 6f has an even higher set of micromechanical characteristics, as it consisted of fine acicular martensite and soft austenite. The microstructure of Figure 6g has a complex composition and includes pearlite, austenite, and carbide inclusions with a developed interfacial surface. The microstructure of Figure 6h consists of matrix austenite and sparse, coarse martensite needles.

The only microstructure with decomposition products of austenite (eutectoid) is the microstructure in Figure 6i. It also showed a large number of non-metallic inclusions.

3.3. Grain Size of Deposited Metal

Figure 7 shows photos of the microstructure of the deposited metal made at the modes specified in Table 3 and the grain size indication.

Figure 8 illustrates histograms of the distribution of grain size in the deposited metal by their nominal size.

Table 6 shows the data on grain morphology in the deposited metal.

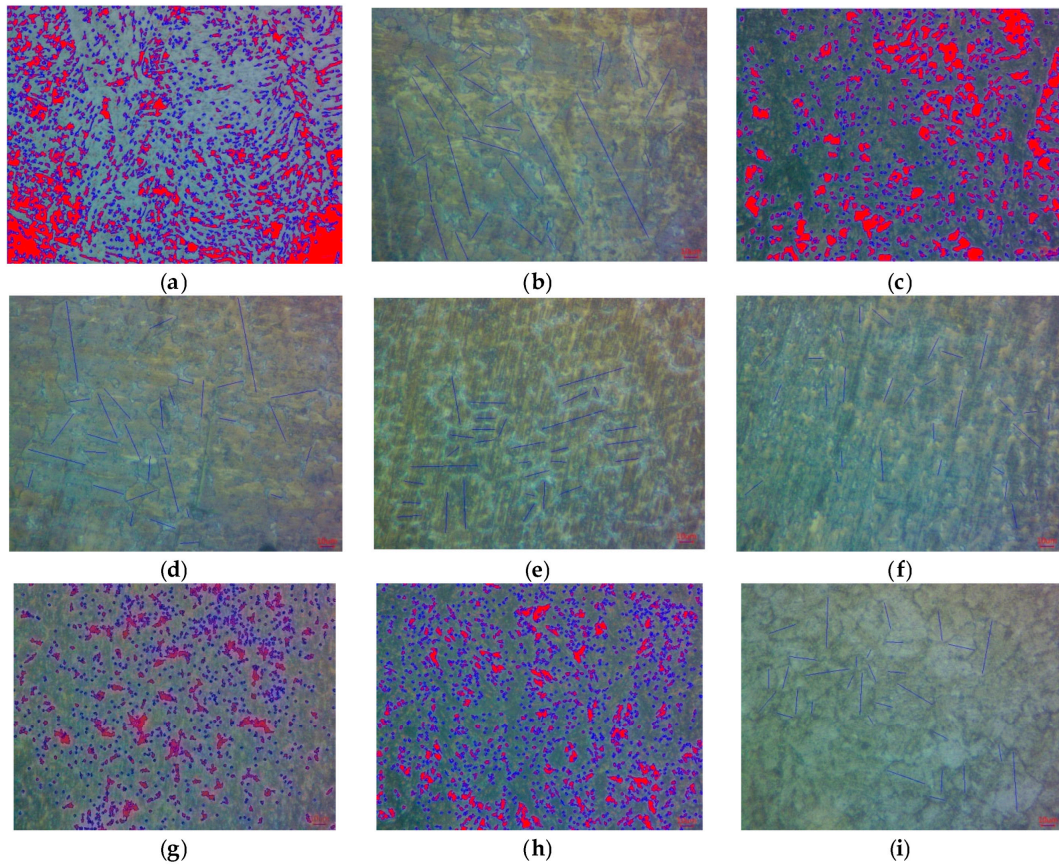


Figure 7. The grain size of the deposited metal, $\times 200$: (a) Exp. 1, (b) Exp. 2, (c) Exp. 3, (d) Exp. 4, (e) Exp. 5, (f) Exp. 6, (g) Exp. 7, (h) Exp. 8, (i) Exp. 9.

Table 6. Grain morphology of the studied samples of deposited metal.

No.	Number of Grains	Grain Size [μm]		
		Average	Minimum	Maximum
1	1291	5.1	0.9	86.1
2	30	35.3	7.9	133.8
3	765	0.9	63.5	5.2
4	31	27.1	7.1	79.9
5	30	24.4	8.2	57.4
6	31	16.8	7.0	31.9
7	1009	3.5	0.9	31.3
8	1421	3.5	0.9	26.6
9	31	22.5	8.1	51.1

Table 7 presents the experimental of grain size (GS) resulting from hardfacing with the developed self-shielded flux-cored wire (FCAW-S) containing an exothermic addition (EA) of $\text{MnO}_2\text{-Al}$ in the filler.

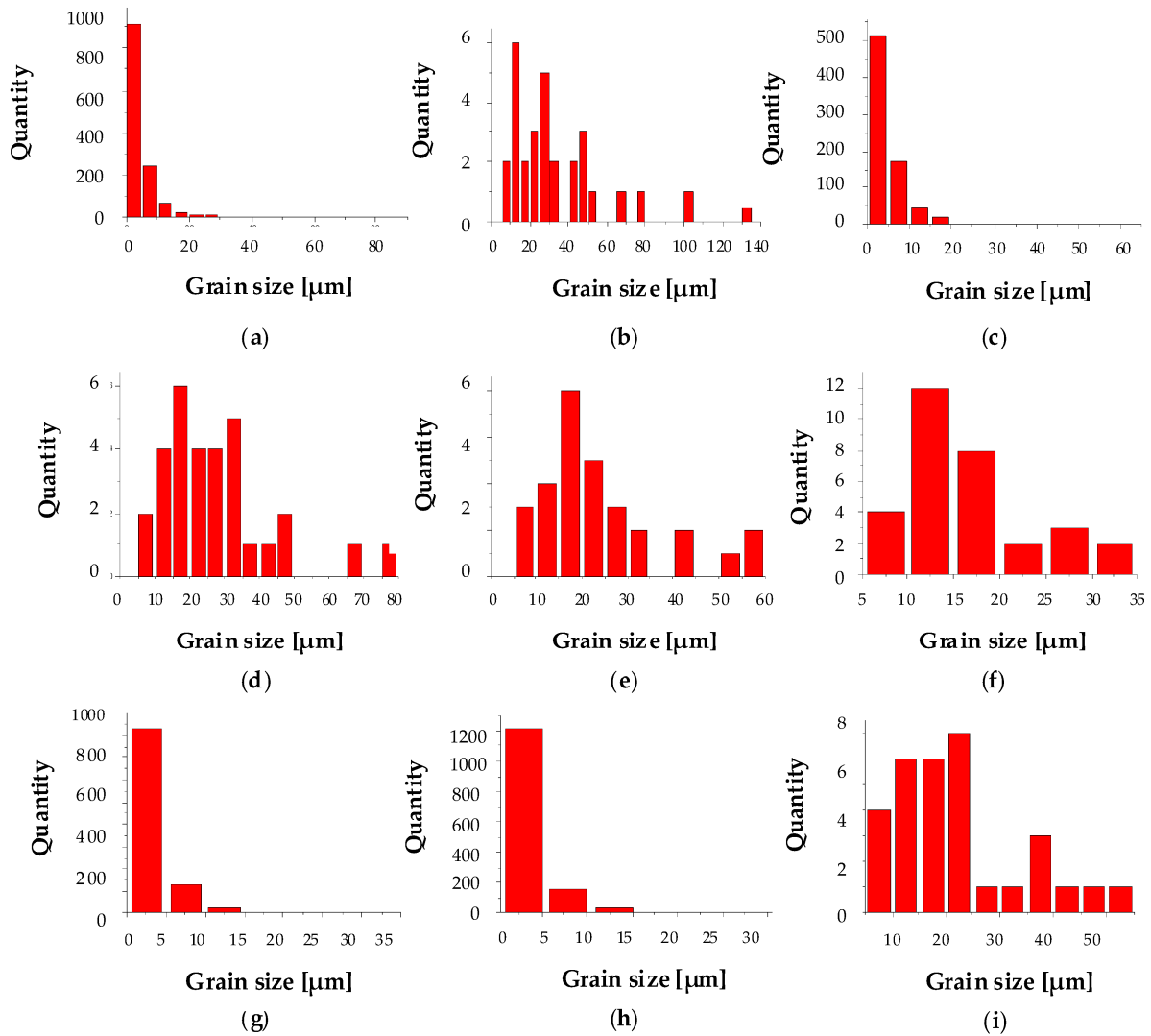


Figure 8. Histogram of the distribution of grain size in the deposited metal by their nominal size depending on the hardfacing mode: (a) Exp. 1, (b) Exp. 2, (c) Exp. 3, (d) Exp. 4, (e) Exp. 5, (f) Exp. 6, (g) Exp. 7, (h) Exp. 8, (i) Exp. 9.

Table 7. Experimental (e) and calculated (c) values of grain size.

№	Grain Size			
	GS (e) [μm]	GS (c) [μm]	Diff. [μm]	Dev. [%]
1	5.10	4.92	0.18	0.04
2	35.30	24.24	11.06	0.31
3	0.90	5.57	−4.67	−5.19
4	27.10	23.01	4.09	0.15
5	24.40	27.71	−3.31	−0.14
6	16.80	27.85	−11.05	−0.66
7	3.50	3.52	−0.02	−0.01
8	3.50	2.92	0.58	0.17
9	22.50	19.37	3.13	0.14

3.3.1. Analyses of Variance for Grain Size

Figure 9 shows the effect of hardfacing parameters on grain size.

The analysis of the pie chart data showed that the grain size (GS) of the deposited metal was significantly influenced by the contact tip to work distance (CTWD) (contribution

of 45.35%). The travel speed and wire feed speed had a lesser impact. Their contribution was 27.82% and 19.63%, respectively. The influence of such a parameter as the set voltage on the power source was significantly small, so it was not taken into account when building mathematical models.

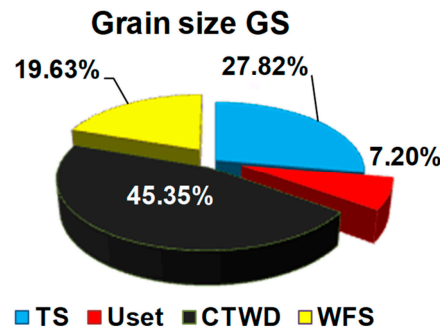


Figure 9. Pie chart of the effect of hardfacing modes on grain size.

3.3.2. Analyses Taguchi for Grain Size

Figure 10 shows the experimental results of the calculated S/N ratios for grain size using the Taguchi method.

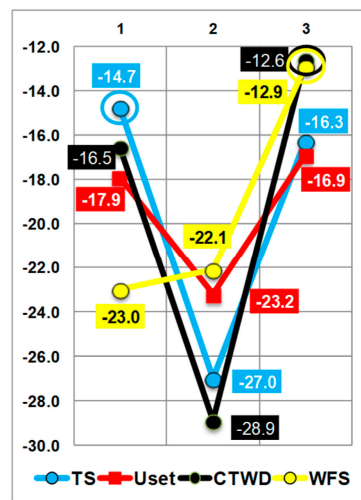


Figure 10. Diagram of main effects for the S/N ratio for grain size characteristics GS.

Analyzing the diagram of the S/N ratio for the grain size indicator, it could be noted that the optimal hardfacing in terms of obtaining the minimum grain size in the hardfacing should be performed at the maximum contact tip to work distance, $CTWD = 50$ mm, high travel speed at low or high values ($TS = 0.27 \text{ m}\cdot\text{min}^{-1}$ or $TS = 0.69 \text{ m}\cdot\text{min}^{-1}$), and wire feed speed at a high level ($WFS = 2.73 \text{ m}\cdot\text{min}^{-1}$).

3.3.3. Development of a Mathematical Model (Box–Hunter) for Grain Size

The equation of the obtained regression model for grain size is provided in Equation (8):

$$\begin{aligned}
 Y(GS) = & 15.273 + 4.44 \cdot TS^2 + 19.889 \cdot CTWD^2 - 13.528 \cdot WFS - 5.19 \cdot WFS^2 - \\
 & - 18.968 \cdot TS \cdot CTWD^2 + 2.028 \cdot TS \cdot WFS^2 - 13.053 \cdot CTWD \cdot WFS^2; \quad (8) \\
 R^2 = & 0.99952.
 \end{aligned}$$

The statistical significance and the degree of influence of each factor on the dependent variables are presented by the Pareto chart in Figure 11a. To evaluate the quality of the constructed mathematical model, a graph of the observed and predicted values of the

influence of each factor on the dependent variables was obtained, which is shown in Figure 11b.

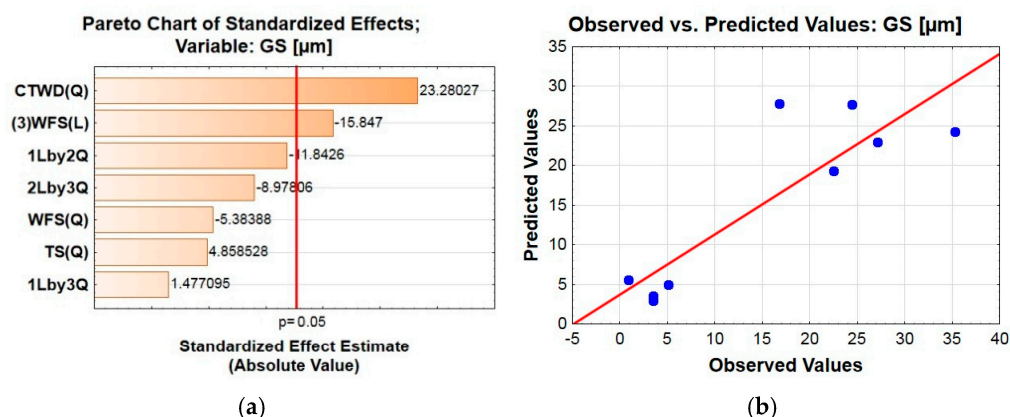


Figure 11. Pareto chart (a) and observed and predicted values of the dependent variable (b) for grain size.

The analysis of the Pareto chart in Figure 11a shows that the significant parameters of the hardfacing mode in terms of their influence on the grain size (GS) are the contact tip to work distance (CTWD) and the wire feed speed (WFS). The analysis of Figure 11b shows the high accuracy of the predicted values for the constructed mathematical model.

Figure 12 shows the response surfaces of the mathematical models of the dependence of grain size on hardfacing modes.

The effect of hardfacing modes on grain size showed an excellent result depending on the combination of parameters. An increase in both mode parameters, both the travel speed in combination with the contact tip to work distance (Figure 12a) as well as the travel speed and wire feed rate (Figure 12c), led to a decrease in the grain size of the deposited metal. This could be explained by the fact that in the heat input calculation formula, the travel speed appeared in the denominator. A different pattern of influence on grain size was observed for the combination of contact tip to work distance and wire feed speed, as shown in Figure 12b: the grain size tended to decrease with increasing contact tip to work distance and decreasing wire feed speed, which was directly proportional to the welding current and appeared in the numerator of the heat input formula.

3.4. Non-Metallic Inclusions

For the metallographic studies, the NMIs were produced in a polished finish (without etching). Digital photographs were taken and uploaded into the Digimizerver 4.6.1 software, where, using a scale bar, pixel values were converted into micrometers. Subsequently, binarization and mask overlaying on the analyzed objects were performed, followed by statistical analysis of the area, perimeter, and linear dimensions of the inclusions. Figure 13 shows the macrostructures of non-metallic inclusions in the deposited metal.

To analyze the chemical composition of non-metallic inclusions, an additional analysis was performed by EDS. Energy dispersive X-ray spectrometer INCA ENERGY 350 with microanalytical INCA X-stream processor, Microscope Image Capture System (MICS), and Inca Energy software. Figure 14 shows the results of the studies.

The analysis of the obtained data showed that non-metallic inclusions in FCAW-S hardfacing with exothermic addition are composite inclusions consisting of oxides (mainly of the corundum type, Al_2O_3) and manganese sulfides (MnS). The presence of the former in the weld metal can be explained by the exothermic reaction $MnO_2 + Al = Mn + Al_2O_3$. The latter have a metallurgical origin, resulting from the unavoidable presence, primarily in the metal sheath of flux-cored wires. As reported by Matsuoka et al. [42], manganese

sulfide possessed better ductility and weak deformation resistance than alumina. However, MnS inclusions possess slightly lower but similar mechanical properties to the matrix [43]. Whereas alumina inclusions will act as hardening particles, thereby enhancing the mechanical properties of the weld metal.

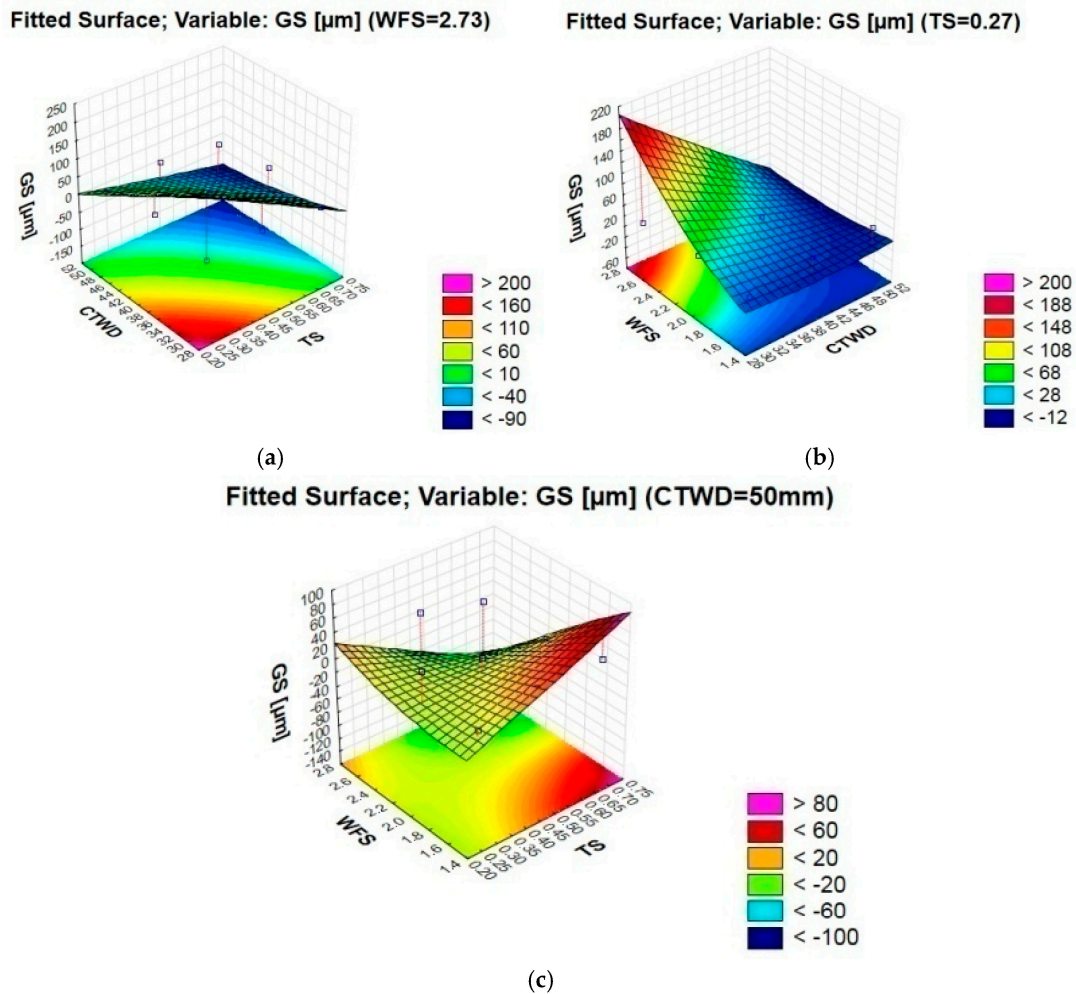


Figure 12. Response surfaces of the mathematical model of grain size dependence on hardfacing modes.

Table 8 shows the size parameters of non-metallic inclusions in the deposited metal.

Table 8. Characteristics of non-metallic inclusions in the deposited metal.

No.	Number of NMIs	Average Area, μm ²	Average Perimeter, μm	Length, μm		
				Average	Min	Max
1	2816	8.9	11.6	4.3	81.2	115.9
2	1971	12.2	13.4	4.5	0.9	110.8
3	1483	25.8	77.9	17.9	1.1	555.0
4	617	17.6	19.9	6.8	1.2	67.2
5	214	9.3	12.3	4.5	1.1	21.1
6	229	19.0	18.5	6.2	1.2	118.7
7	589	9.5	12.9	4.9	1.2	109.4
8	128	14.9	14.1	5.3	1.2	39.4
9	429	15.9	14.1	5.0	1.2	59.0

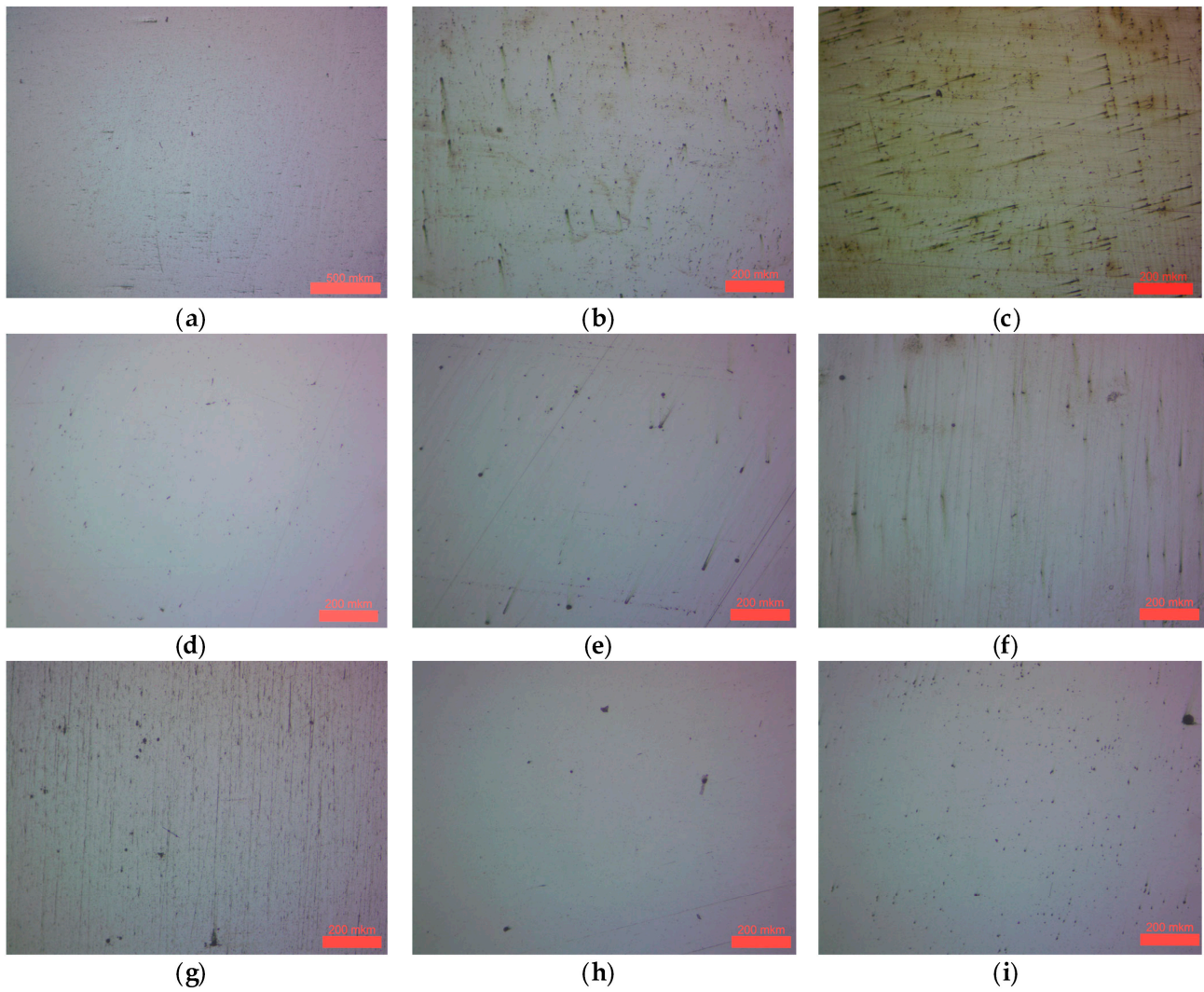


Figure 13. Non-metallic inclusions in the deposited metal, $\times 200$: (a) Exp. 1, (b) Exp. 2, (c) Exp. 3, (d) Exp. 4, (e) Exp. 5, (f) Exp. 6, (g) Exp. 7, (h) Exp. 8, (i) Exp. 9.

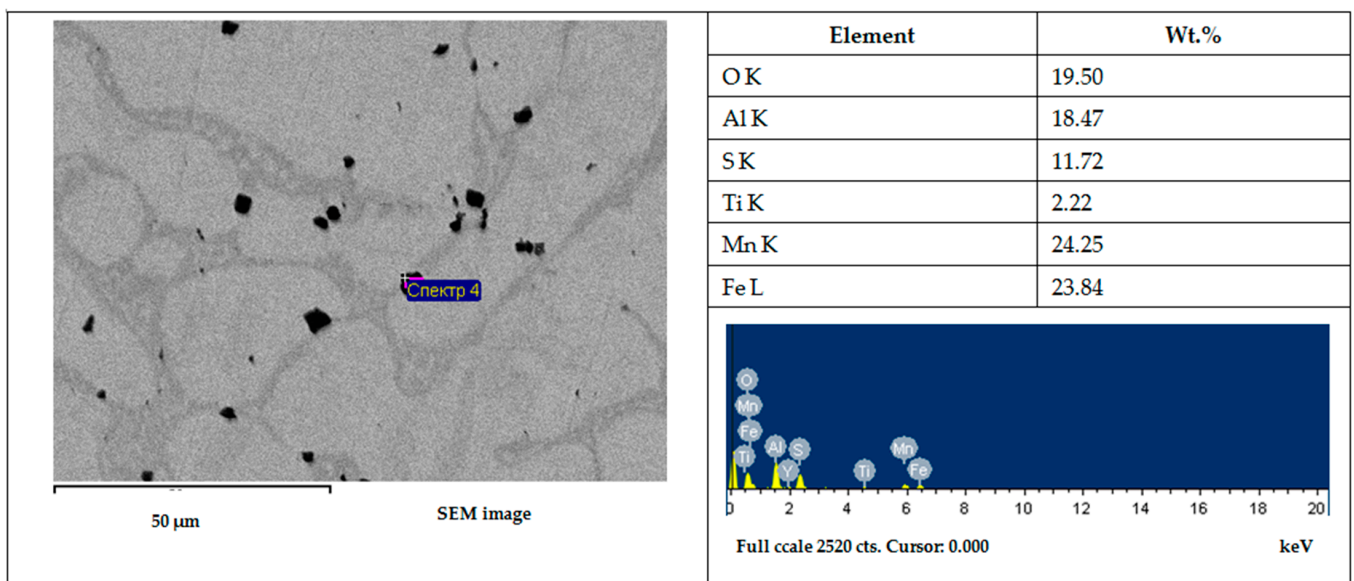


Figure 14. SEM-EDX analysis of non-metal inclusions in deposited metal 140MnCrTi10-3.

3.4.1. Analyses of Variance for Non-Metallic Inclusions (NMIs)

Table 9 shows the size of non-metallic inclusions in the deposited metal.

Table 9. Morphological characteristics of non-metallic inclusions in deposited metal samples that have been deposited under different modes of deposition.

№	Number of Nonmetal Inclusions				Average Area			
	$N_{NMI} (e)$ [pcs]	$N_{NMI} (c)$ [pcs]	Diff. [pcs]	Dev.	$S_{NMI} (e)$ [μm^2]	$S_{NMI} (c)$ [μm^2]	Diff. [μm^2]	Dev.
1	2816	2840.45	-24.45	-0.01	12.2	13.48	-1.28	-0.11
2	1971	1922.85	48.15	0.02	25.8	26.21	-0.41	-0.02
3	1483	1506.71	-23.71	-0.02	17.6	17.19	0.41	0.02
4	617	633.59	-16.59	-0.03	9.3	10.17	-0.87	-0.09
5	214	181.33	32.67	0.15	19.0	17.07	1.93	0.10
6	229	245.08	-16.08	-0.07	9.5	10.41	-0.91	-0.10
7	589	547.97	41.03	0.07	14.9	13.48	1.42	0.10
8	128	208.82	-80.82	-0.63	15.9	17.06	-1.17	-0.07
9	429	389.21	39.79	0.09	8.9	8.03	0.87	0.10

№	Maximum length				Average length			
	$LL_{NMI} (e)$ [μm]	$LL_{NMI} (c)$ [μm]	Diff. [μm]	Dev.	$L_{NMI} (e)$ [μm]	$L_{NMI} (c)$ [μm]	Diff.	Dev.
1	115.9	112.71	3.19	0.03	4.30	4.81	-0.51	-0.20
2	110.8	111.26	-0.46	-0.00	4.50	5.40	-0.90	0.01
3	555.0	555.19	-0.19	0.00	17.90	17.74	0.16	-0.02
4	67.2	67.01	0.19	0.00	6.80	6.96	-0.16	0.11
5	21.1	24.29	-3.19	-0.15	4.50	3.99	0.51	0.10
6	118.7	119.68	-0.98	-0.01	6.20	5.56	0.64	0.19
7	109.4	95.86	13.54	0.12	4.90	3.98	0.92	-0.02
8	39.4	69.07	-29.67	-0.75	5.30	5.40	-0.10	-0.11
9	59.0	41.44	17.56	0.30	5.00	5.56	-0.56	-0.12

(e) and (c) are necessary to distinguish between data obtained experimentally and those predicted using the developed model.

Figure 15 shows the effect of the hardfacing modes parameters (travel speed, set voltage on the power source, contact tip to work distance, and wire feed speed) on the characteristics of non-metallic inclusions: their number (N_{NMI}), average area (S_{NMI}), maximum length (LL_{NMI}), and average length (L_{NMI}).

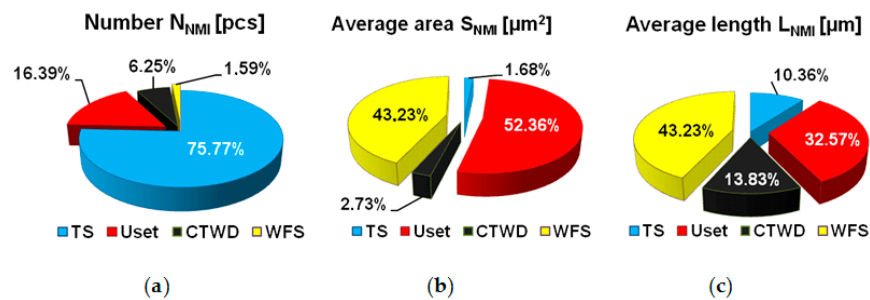


Figure 15. Pie charts of the influence of hardfacing mode parameters on NMI parameters: (a) number of NMIs (N_{NMI}); (b) average area of NMIs (S_{NMI}); (c) average length of NMIs (L_{NMI}).

Studying the pie charts allowed us to conclude that the dominant parameter influencing the value of the number of non-metallic inclusions (N_{NMI}) in the deposited metal was the travel speed (TS) (contribution of 75.8%). The set arc voltage had a much smaller effect on the N_{NMI} (contribution of 16.4%). Other mode parameters did not affect the N_{NMI} parameter.

The average area (S_{NMI}) and the average length (L_{NMI}) of non-metallic inclusions depended on the value of the wire feed speed (contributions of 43.2% for each parameter),

as well as the set arc voltage (contributions of 52.4% and 32.6%, respectively). The average length (L_{NMI}) was slightly influenced by the contact tip to work distance ($CTWD$) (contribution of 13.8%), while the travel speed had no effect. There was no effect of $CTWD$ and TS on the average area (S_{NMI}).

3.4.2. Taguchi Analyses for Non-Metallic Inclusions

For preliminary optimization of hardfacing modes, a study was performed, the results of which are presented in Figure 16, which showed the calculation of the S/N ratio for the NMI indicators using the Taguchi method. For preliminary optimization of hardfacing modes, a study was performed, the results of which are shown in Figure 16, showing the calculation of the S/N ratio for the NMI indicators using the Taguchi method.

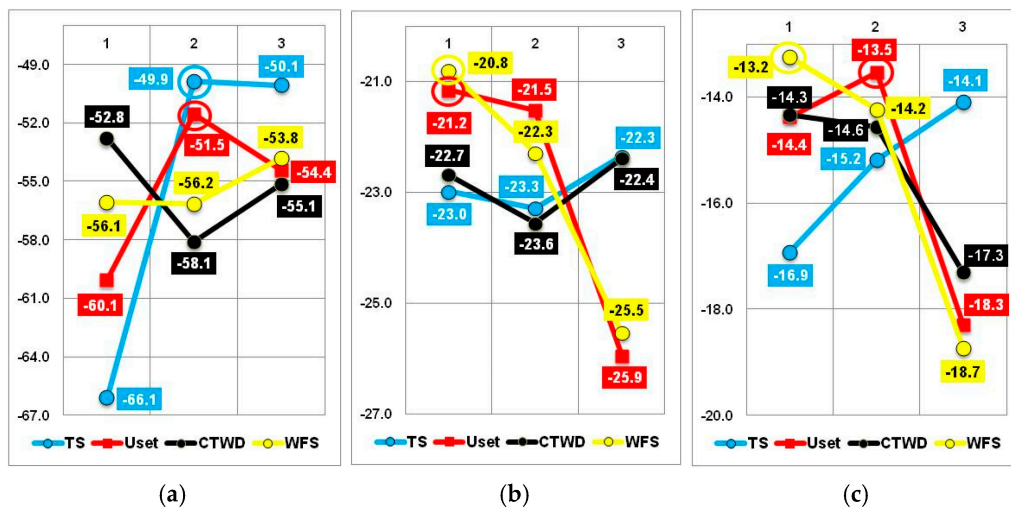


Figure 16. Diagram of the main effects of the S/N ratio for the characteristics of non-metallic inclusion parameters: (a) number of NMIs (N_{NMI}); (b) average area of NMIs (S_{NMI}); (c) average length of NMIs (L_{NMI}).

Figure 16a shows that the lowest number and maximum and average length of non-metallic inclusions could be obtained at a travel speed (TS) at medium and high levels ($TS = 2.07 \text{ m}\cdot\text{min}^{-1}$ and $TS = 2.73 \text{ m}\cdot\text{min}^{-1}$), as well as at the set arc voltage at the second level ($U_{set} = 29.2 \text{ V}$). The smallest area of non-metallic inclusions was provided when hardfacing at the minimum levels of the set arc voltage ($U_{set} = 26.0 \text{ V}$) and wire feed speed ($WFS = 1.50 \text{ m}\cdot\text{min}^{-1}$).

The analysis of the diagrams of the main effects of the S/N ratio (see Figure 16a–c) showed that in terms of obtaining the minimum values of the number (N_{NMI}), the area (S_{NMI}), and the length (LL_{NMI} and L_{NMI}) of non-metallic inclusions, the optimal hardfacing modes would be the following: travel speed, $TS = 0.47 \text{ m}\cdot\text{min}^{-1}$; set voltage on the power source, $U_{set} = 29.2 \text{ V}$; contact tip to work distance, $CTWD = 30 \text{ mm}$; and $WFS = 1.50 \text{ mm}\cdot\text{min}^{-1}$.

3.4.3. Development of a Mathematical Model (Box–Hunter) for Non-Metallic Inclusions NMI

The developed mathematical models of non-metallic inclusion characteristics are presented in Equations (9)–(12).

$$Y(N_{NMI}) = 923.45 - 1704.99 \cdot TS - 931.9 \cdot TS^2 - 615.48 \cdot U_{set} - 260.99 \cdot U_{set}^2 + 587.49 \cdot TS \cdot U_{set} + 196.15 \cdot TS^2 \cdot U_{set} \quad (9)$$

$$Y(S_{NMI}) = 16.18 + 7.97 \cdot U_{set} + 11.15 \cdot WFS - 3.27 \cdot WFS^2 + 3.44 \cdot U_{set}^2 \cdot WFS \quad (10)$$

$$Y(LL_{NMI}) = 197.02 - 185.41 \cdot TS^2 + 387.02 \cdot U_{set} + 287.99 \cdot WFS - 228.18 \cdot WFS^2 - 436.354 \cdot TS \cdot U_{set} + 671.48 \cdot TS \cdot WFS \tag{11}$$

$$Y(L_{NMI}) = 9.19 + 7.62 \cdot U_{set} + 0.02 \cdot U_{set} - 5.71 \cdot WFS^2 - 5.21 \cdot U_{set} \cdot WFS^2 + 5.26 \cdot U_{set} \cdot WFS \tag{12}$$

Table 10 presents the regression coefficients for each response.

Table 10. Result of dispersion analysis for the applied models of parameters characterizing non-metallic inclusions in deposited metal samples.

Parameter	Coefficient of Determination R-Sqr	Adjusted Sum of Squares (SS)	Model Quality
Number of nonmetal inclusions (N_{NMI})	0.99789	0.99157	Very good
Average area (S_{NMI})	0.9649	0.92981	Good
Maximum length (LL_{NMI})	0.99337	0.9735	Very good
Average length (L_{NMI})	0.99298	0.98127	Very good

The statistical significance and the degree of influence of each factor on the dependent variables are represented by Pareto charts in Figure 17.

Consideration of the obtained Pareto charts made it possible to conclude that the main significant hardfacing modes were the travel speed, the set arc voltage, and the wire feed speed. The analysis of Figure 17 of the graphs of the observed and predicted values of the dependent variable showed high accuracy for all the constructed mathematical models.

Figure 18 shows the 3D response surfaces of the developed mathematical models.

As shown in Figures 15a and 18a, the total number of NMIs would be affected by the travel speed. This could be explained by the lifetime of the weld pool. The higher the travel speed, the lower the heat input and thus the weld pool lifetime. The size of the latter was also determined by the volume of molten electrode metal, which was determined by the wire feed speed. Whereas the size of the NMIs was influenced by such welding parameters as the set voltage on the power source and the wire feed speed.

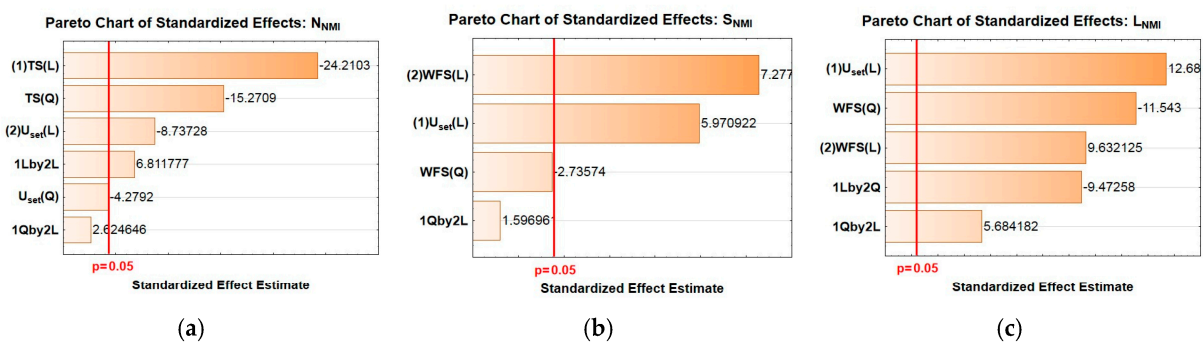


Figure 17. Pareto charts: (a) number of NMIs (N_{NMI}); (b) average area of NMIs (S_{NMI}); and (c) average length of NMIs (L_{NMI}).

3.5. Mechanical Properties

Table 11 shows the experimental and calculated (obtained from the equations of the mathematical model) values of HRA hardness measured after hardfacing with the developed FCAW-S with exothermic addition (EA) of MnO_2 -Al in the filler. The hardness was determined using the standard Rockwell method according to the A scale (HRA) of ISO 6508-1.

Table 11. Experimental (e) and calculated (c) values of HRA hardness.

№	N Specimen	Hardness			
		HRA (e)	HRA (c)	Diff.	Dev.
1	P5-E1-1	62.00	60.04	1.96	0.03
2	P5-E1-2	61.00	63.25	−2.25	−0.04
3	P5-E1-3	58.00	57.72	0.28	0.01
4	P5-E1-4	69.00	67.55	1.45	0.02
5	P5-E1-5	69.00	69.56	−0.56	−0.01
6	P5-E1-6	72.00	72.89	−0.89	−0.01
7	P5-E1-7	79.00	75.86	3.14	0.04
8	P5-E1-8	69.00	70.73	−1.73	−0.03
9	P5-E1-9	71.00	72.40	−1.40	−0.02

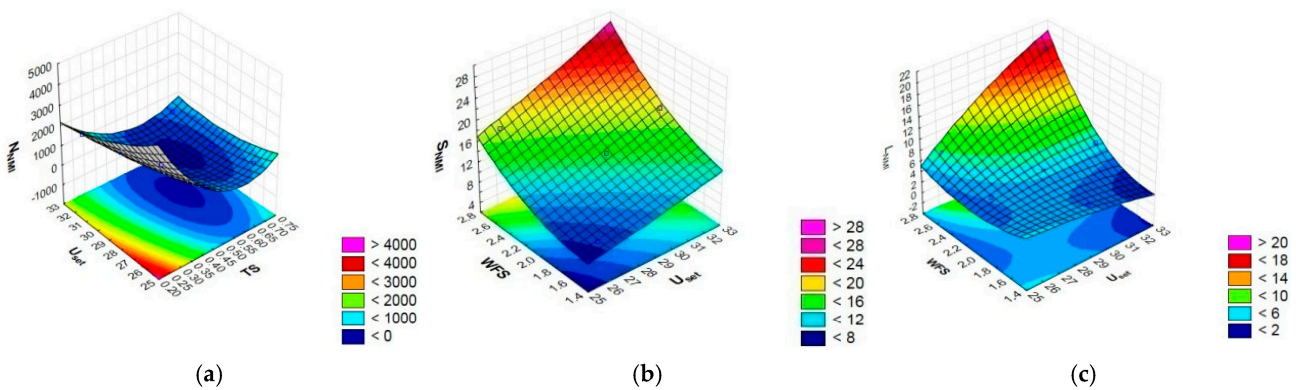


Figure 18. Response surfaces of the mathematical model of the dependence of non-metallic inclusion morphology indicators: (a) number of NMIs (N_{NMI}); (b) average area of NMIs (S_{NMI}); and (c) average length of NMIs (L_{NMI}).

It is known that the austenitic phase in high-manganese steels corresponds to a hardness of 190–220 HB (56–64 HRA) [44]. The analysis showed that the deposited metal of indices P5-E1-7 had the lowest hardness of 79 HRA. This can be explained by the large proportion of the pearlite phase in the matrix. This sample is characterized by the highest cooling rate, $CR = 9.34 \text{ }^\circ\text{C}\cdot\text{s}^{-1}$, which is the main reason for the appearance of pearlite in the structure of the weld metal. The lower hardness of the samples with indices P5-E1-1, P5-E1-2, and P5-E1-3 is explained by the low travel speed. The lowest hardness was observed for the sample for which the thermal welding cycle had the lowest cooling rate, $CR = 2.53 \text{ }^\circ\text{C}\cdot\text{s}^{-1}$.

3.5.1. Analyses of Variance and Taguchi for Hardness

Figure 19 shows the contribution of each of the hardfacing mode parameters to the hardness and S/N ratio at each level.

According to Figure 19a, the main influence on hardness was exerted by the travel speed (contribution was 81.19%). The wire feed speed (WFS) also had an effect. The effect of other mode parameters was not significant, so their influence could be neglected.

Analysis of the graph in Figure 19b showed that the optimum conditions for obtaining the lowest hardness of the high-manganese alloy inherent in the austenitic matrix would be achieved at a low travel speed ($TS = 0.27 \text{ m}\cdot\text{min}^{-1}$) and at a high wire feed speed ($WFS = 2.73 \text{ m}\cdot\text{min}^{-1}$).

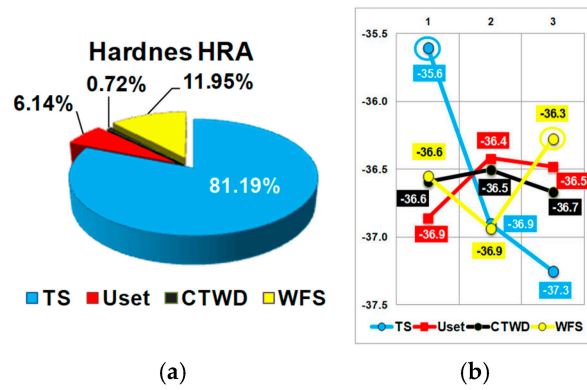


Figure 19. Pie chart of the influence of hardfacing modes on hardness (a) and the main effects diagram for the S/N ratio for hardness (b).

3.5.2. Development of a Mathematical Model (Box–Hunter) for Hardness

The equation of the obtained regression model for hardness is provided in Equation (13):

$$Y(HRA) = 67.875 + 12.667 \cdot TS + 3.706 \cdot TS^2 - 2 \cdot WFS + 4.331 \cdot WFS^2 + 4.035 \cdot TS \cdot WFS^2; \tag{13}$$

$$R^2 = 0.98386.$$

The statistical significance and the degree of influence of each factor on hardness is represented by the Pareto chart in Figure 20a. To evaluate the quality of the constructed mathematical model, a graph of the observed and predicted values of the influence of each factor on hardness is plotted in Figure 20b.

The analysis of the Pareto chart of Figure 20a showed that in terms of the influence of hardfacing modes on the HRA hardness value, the most significant were the travel speed (TS) and the wire feed speed (WFS). This was confirmed by the results of the ANOVA analysis. The developed mathematical model in Figure 20b shows the high accuracy of the predicted values.

Figure 21 shows the response surface of the mathematical model of the dependence of the hardness of the deposited metal on the hardfacing modes.

The 3D surface of the hardness dependence on the significant parameters of the hardfacing mode for the developed mathematical model showed that the desired level of mechanical properties would correspond to a travel speed at a low level $TS \leq 0.4 \text{ m} \cdot \text{min}^{-1}$.

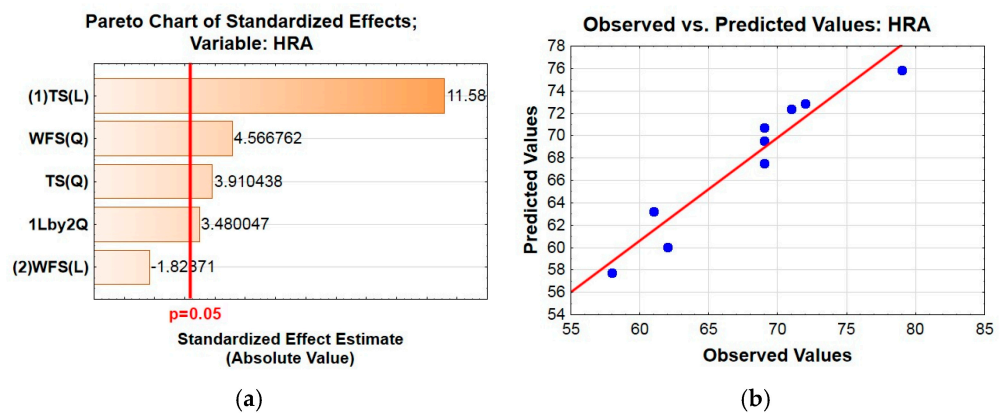


Figure 20. Pareto chart (a) and observed and predicted values of the dependent variable (b) for HRA gardness.

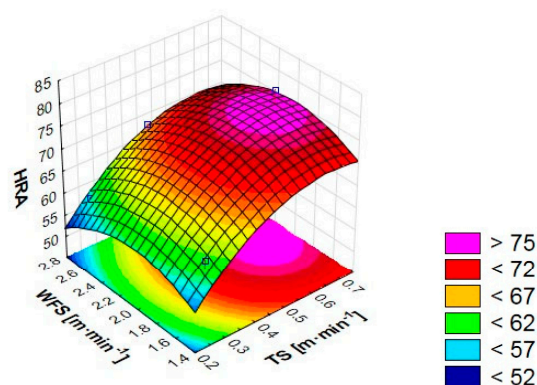


Figure 21. The response surface of the mathematical model of the dependence of HRA hardness on hardfacing modes.

4. Discussion

Our studies have shown a significant effect of welding modes on the microstructure of the deposited metal and its mechanical properties, made by flux-cored wire with a high-energy exothermic MnO_2 -Al addition under different hardfacing modes.

It should be noted that for the considered ranges of changes in the parameters of the hardfacing modes, the greatest influence on the microstructure and mechanical properties was exerted by the travel speed (TS) and wire feed speed (WFS). At the same time, the quality of the deposited metal, characterized by the content and morphology of non-metallic inclusions, was most affected by such parameters of the hardfacing modes as wire feed speed and arc voltage. The amount of NMIs was most affected by the travel speed, which could be explained by the rapid solidification of the weld pool. As a result, the NMIs did not have time to float up and transfer into weld slag.

The main reason for the reduction in grain size was the decreased lifetime of the molten weld pool, which was primarily influenced by the travel speed (TS) and wire feed speed (WFS). These parameters of the hardfacing mode affected the cooling rate and the weld pool lifetime. This ultimately affected the degree of removal of small-sized non-metallic inclusions. Small-sized non-metallic inclusions served as centers of crystallization and refined grains. These inclusions lowered the energy barrier for crystal formation and acted as focal points around which metal atoms arranged themselves into a crystalline lattice. Thus, the hardfacing modes directly influenced the size and cooling rate of the weld pool and the amount of small-sized NMIs. The study by Wang et al. [45] showed that the total number of NMIs and their size were affected by the presence of an exothermic mixture. The main effect was an increase in their total number and average size. While the study by Trembach et al. [24] demonstrated that the presence of an exothermic addition in the filler increased the number of non-metallic inclusions in the deposited metal and reduced their size.

In addition, in some hardfacing modes, there were cases when the exothermic reaction took place at the weld pool stage. This resulted in the ingress of the exothermic addition components (namely MnO_2 and Al) in their original form into the molten weld pool.

The results showed that lower travel speeds corresponded to higher hardness values. This was due to the lower cooling rate and, accordingly, the formation of harder structural components than primary austenite. This tendency was typical for high-manganese, high-carbon alloys such as Hadfield steel. This corresponded to a high level of travel speed and wire feed speed.

Further studies will be conducted to investigate the effect of hardfacing modes on the tribological properties of the deposited metal.

The average linear size NMI and hardness were selected as final parameters of the hardfacing process modes. The first parameter is mainly influenced by such investigated parameters as wire feed speed, set voltage on the power source, and, to a small extent, contact tip to work distance. Whereas the hardness parameter is mainly influenced by travel speed. Based on the previously obtained optimal levels of variables for the selected output parameters, there will be the following values: travel speed, $TS = 0.27 \text{ m}\cdot\text{min}^{-1}$; set voltage on the power source, $U_{\text{set}} = 29.2 \text{ V}$; contact tip to work distance, $CTWD = 30 \text{ mm}$; and $WFS = 1.50 \text{ mm}\cdot\text{min}^{-1}$.

5. Conclusions

In this work we have investigated the influence of hardfacing modes on the parameters of the thermal cycle of welding, as well as the effect on the properties of weld metal samples of high-manganese, high-carbon alloys of the FeMnCrTi system (microstructure, non-metallic inclusions, grain size, and hardness). The hardfacing process was carried out using self-shielded flux-cored wire with high-energy exothermic addition in the filler of the MnO_2Al system. In the above study, a new technique with an orthogonal experimental plan, L9 was used. Based on the obtained results, the following conclusions can be drawn:

1. The thermal cycle parameters and hardness will mainly be influenced by the travel speed variable. The influence of other parameters is low or not significant.
2. It was determined that for flux-cored wires with an exothermic addition, the size of the deposited metal grain size is most affected by the contact tip to work distance (CTWD), to a lesser extent, by the travel speed (TS) and the wire feed speed (WFS).
3. The analysis of the deposited metal samples showed that the size of NMIs was influenced by the wire feed speed and the set voltage on the power source.
4. As a result of the study, the optimum hardfacing modes were determined, which will provide minimum NMI size, fine grain, and high hardness of the austenitic phase with the following: $TS = 0.27 \text{ m}\cdot\text{min}^{-1}$, $U_{\text{set}} = 29.2 \text{ V}$, $CTWD = 30 \text{ mm}$, and $WFS = 1.50 \text{ mm}\cdot\text{min}^{-1}$.

Author Contributions: Conceptualization, I.T. and B.T.; methodology, I.T.; validation, I.T., O.B. (Olha Babych) and Y.M.; formal analysis, A.G., M.K. and B.T.; investigation, I.T. and S.K.; resources, I.T.; data curation, I.T., B.T. and O.B. (Oleksii Balenko); writing—original draft preparation, B.T. and I.T.; writing—review and editing, I.T., Y.M. and O.V.; visualization, I.T., B.T., S.K. and A.P.; supervision, A.G.; project administration, B.T. and N.M. All authors have read and agreed to the published version of the manuscript.

Funding: This research received no external funding.

Institutional Review Board Statement: Not applicable.

Informed Consent Statement: Not applicable.

Data Availability Statement: Data are contained within the article.

Conflicts of Interest: Author Bohdan Trembach was employed by the company Rappresentanze Industriali M&C Division doo. The remaining authors declare that the research was conducted in the absence of any commercial or financial relationships that could be construed as a potential conflict of interest.

References

1. Ulbrich, D.; Stachowiak, A.; Kowalczyk, J.; Wieczorek, D.; Matysiak, W. Tribocorrosion and Abrasive Wear Test of 22MnCrB5 Hot-Formed Steel. *Materials* **2022**, *15*, 3892. [[CrossRef](#)] [[PubMed](#)]
2. Ulbrich, D.; Psuj, G.; Bartkowski, D.; Bartkowska, A. Assessment of Coating Properties in Car Body by Ultrasonic Method. *Appl. Sci.* **2024**, *14*, 8117. [[CrossRef](#)]
3. Spišák, E.; Kaščák, L.; Viňáš, J. Research into properties of joints of combined materials made by resistance spot welding. *Chemické listy* **2011**, *105*, 488–490.

4. Riabov, I.; Goolak, S.; Neduzha, L. An Estimation of the Energy Savings of a Mainline Diesel Locomotive Equipped with an Energy Storage Device. *Vehicles* **2024**, *6*, 611–631. [[CrossRef](#)]
5. Zhang, T.; Yang, K.; Zhu, Z.; Xu, L.; Chen, G.; Fang, N.; Kou, S. Effect of Cr and W on microstructure and wear resistance of arc additive manufactured flux-cored wire for railway wheels. *J. Mater. Res. Technol.* **2024**, *30*, 3438–3447. [[CrossRef](#)]
6. Krbata, M.; Kohutiar, M.; Escherova, J.; Klučiar, P.; Studeny, Z.; Trembach, B.; Beronská, N.; Breznická, A.; Timárová, L. Continuous Cooling Transformation of Tool Steels X153CrMoV12 and 100MnCrW4: Analysis of Microstructure and Hardness Changes. *Appl. Mech.* **2025**, *6*, 16. [[CrossRef](#)]
7. Cunha, M.C.; Oliveira, H.R.; Oliveira, A.; Souza, M.C.C. Microstructural and wear investigation of FeCrC and FeCrC-NbBhardfacing alloys deposited with FCAW-S. *Int. J. Adv. Manuf. Technol.* **2024**, *136*, 1241–1251. [[CrossRef](#)]
8. Chabak, Y.G.; Golinskyi, M.A.; Efremenko, V.G.; Halfa, H.; Zurnadzhy, V.I.; Efremenko, B.V.; Tsvetkova, E.V.; Dzherenova, A.V. Ti-rich carboborides in the multi-component high-boron alloy: Morphology and elemental distribution. *Phys. Chem. Solid State* **2023**, *24*, 707–713. [[CrossRef](#)]
9. Sukhova, O.V.; Polonsky, V.A. Structure and corrosion of quasicrystalline cast Al–Co–Ni and Al–Fe–Ni alloys in aqueous NaCl solution. *East Eur. J. Phys.* **2020**, *3*, 5–10. [[CrossRef](#)]
10. Prysazhnyuk, P.; Bembenek, M.; Drach, I.; Korzhov, A.; Romanyshyn, L.; Ropyak, L. Restoration of the Impact Crusher Rotor Using FCAW with High-Manganese Steel Reinforced by Complex Carbides. *Manag. Syst. Prod. Eng.* **2024**, *32*, 294–302. [[CrossRef](#)]
11. Hlushkova, D.B.; Bagrov, V.A.; Saenko, V.A.; Volchuk, V.M.; Kalinin, A.V.; Kalinina, N.E. Study of wear of the building-up zone of martensite-austenitic and secondary hardening steels of the Cr-Mn-Ti system. *Probl. At. Sci. Technol.* **2023**, *144*, 105–109. [[CrossRef](#)]
12. Sharma, L.; Chhibber, R.; Kumar, V.; Khan, W.N. Element transfer investigations on silica based Submerged Arc welding fluxes. *Silicon* **2022**, *15*, 301–319. [[CrossRef](#)]
13. Trembach, B.; Balenko, O.; Davydov, V.; Brechko, V.; Trembach, I.; Kabatskyi, O. Prediction the Melting Characteristics of Self-Shielded Flux Cored arc Welding (FCAW-S) with Exothermic Addition (CuO-Al). In Proceedings of the IEEE 4th International Conference on Modern Electrical and Energy System (MEES), Kremenchuk, Ukraine, 20–23 October 2022; pp. 1–6. [[CrossRef](#)]
14. Świerczyńska, A.; Varbai, B.; Pandey, C.; Fydrych, D. Exploring the trends in flux-cored arc welding: Scientometric analysis approach. *Int. J. Adv. Manuf. Technol.* **2024**, *130*, 87–110. [[CrossRef](#)]
15. Liu, Q.; Mi, H.; Feng, L.; Guo, W.; He, B. A critical overview of welding and directed energy deposition with flux-cored wires. *J. Manuf. Process.* **2025**, *142*, 231–268. [[CrossRef](#)]
16. Júnior, J.G.F.; Cardoso, A.H.C.; Bracarense, A.Q. Effects of TiC formation in situ by applying titanium chips and other ingredients as a flux of tubular wire. *J. Braz. Soc. Mech. Sci. Eng.* **2020**, *42*, 375. [[CrossRef](#)]
17. Fagundes, J.G.; Moreno, A.M.; Ribeiro, P.H.; Arias, A.R.; Bracarense, A.Q. Formation of TiC by the application of Ti6Al4V machining chips as flux compounds of tubular wires. *J. Phys. Conf. Ser.* **2018**, *1126*, 012027. [[CrossRef](#)]
18. Lozynskyi, V.; Trembach, B.; Hossain, M.M.; Kabir, M.H.; Silchenko, Y.; Krbata, M.; Sadovyi, K.; Kolomiitse, O.; Ropyak, L. Prediction of phase composition and mechanical properties Fe–Cr–C–B–Ti–Cu hardfacing alloys: Modeling and experimental validations. *Heliyon* **2024**, *10*, e25199. [[CrossRef](#)] [[PubMed](#)]
19. Bembenek, M.; Prysazhnyuk, P.; Shihab, T.; Machnik, R.; Ivanov, O.; Ropyak, L. Microstructure and Wear Characterization of the Fe-Mo-B-C-Based Hardfacing Alloys Deposited by Flux-Cored Arc Welding. *Materials* **2022**, *15*, 5074. [[CrossRef](#)]
20. Shihab, S.T.A.; Prysazhnyuk, P.; Andrusyshyn, R.; Lutsak, L.; Ivanov, O.; Tsap, I. Forming the structure and the properties of electric arc coatings based on high manganese steel alloyed with titanium and niobium carbides. *East.-Eur. J. Enterpr. Technol.* **2020**, *1*, 38–44. [[CrossRef](#)]
21. Brykov, M.N.; Akrytova, T.O.; Osipov, M.J.; Petryshynets, I.; Puchy, V.; Efremenko, V.G.; Shimizu, K.; Kunert, M.; Hesse, O. Abrasive Wear of High-Carbon Low-Alloyed Austenite Steel: Microhardness, Microstructure and X-ray Characteristics of Worn Surface. *Material* **2021**, *14*, 6159. [[CrossRef](#)]
22. Zurnadzhy, V.I.; Efremenko, V.G.; Brykov, M.N.; Petryshynets, I.; Pastukhova, T.V.; Kussa, R.A. The Metastability of Retained Austenite in Multiphase Steel during Abrasive Wear. *J. Frict. Wear* **2020**, *41*, 119–124. [[CrossRef](#)]
23. Luo, Q.; Zhu, J. Wear property and wear mechanisms of High-manganese austenitic hadfield steel in dry reciprocal sliding. *Lubricants* **2022**, *10*, 37. [[CrossRef](#)]
24. Trembach, B.; Grin, A.; Makarenko, N.; Zharikov, S.; Trembach, I.; Markov, O. Influence of the core filler composition on the recovery of alloying elements during the self-shielded flux-cored arc welding. *J. Mater. Res. Technol.* **2020**, *9*, 10520–10528. [[CrossRef](#)]
25. Karimi, M.R.; Wang, S.H.; Jelovica, J. Characterization of cold metal transfer and conventional short-circuit gas metal arc welding processes for depositing tungsten carbide-reinforced metal matrix composite overlays. *Int. J. Adv. Manuf. Technol.* **2023**, *128*, 2551–2570. [[CrossRef](#)]
26. Kim, C.J.; Seo, B.W.; Son, H.J.; Kim, S.; Kim, D.; Cho, Y.T. Slag inclusion-free flux cored wire arc directed energy deposition process. *Mater. Des.* **2024**, *238*, 112669. [[CrossRef](#)]

27. Zhu, Z.; Fan, K.; Liu, H.; Ma, G. Characteristics of short-circuit behaviour and its influencing factors in self-shielded flux-cored arc welding. *Sci. Technol. Weld. Join.* **2016**, *21*, 91–98. [[CrossRef](#)]
28. Park, Y.D.; Kang, N.; Malene, S.H.; Olson, L. Effect of exothermic additions on heat generation and arc process efficiency in flux-cored arc welding. *Met. Mater. Int.* **2007**, *13*, 501–509. [[CrossRef](#)]
29. Trembach, I.O.; Trembach, B.O.; Grin, A.G.; Luzhetskyy, R.Y.; Brechko, V.O.; Zakovorotnyi, O.Y.; Balenko, O.I.; Molchanov, H.I.; Rebrova, O.M.; Kabatskyi, O.V. Application of a complete factorial experiment for optimization of the filling factor and charge density of self-shielding flux-cored powder wire. *Mater. Sci.* **2025**, *60*, 52–59. [[CrossRef](#)]
30. Vlasov, A.F.; Makarenko, N.A. Special features of heating and melting electrodes with an exothermic mixture in the coating. *Weld. Int.* **2016**, *30*, 717–722. [[CrossRef](#)]
31. Li, H.; Hu, C.; Hu, J.; Han, K.; Wang, Z.; Yang, R.; Liu, D. Underwater wet welding of high-strength low-alloy steel using self-shielded flux-cored wire with highly exothermic Al/CuO mixture. *J. Mater. Process. Technol.* **2024**, *328*, 118404. [[CrossRef](#)]
32. Li, H.L.; Liu, D.; Guo, N.; Chena, H.; Dua, Y.P.; Feng, J.C. The effect of alumino-thermic addition on underwater wet welding process stability. *J. Mater. Process. Technol.* **2017**, *245*, 149–156. [[CrossRef](#)]
33. Lozynskiy, V.; Trembach, B.; Katinas, E.; Sadoviy, K.; Krbata, M.; Balenko, O.; Krasnoshapka, I.; Rebrova, O.; Knyazev, S.; Kabatskyi, O.; et al. Effect of Exothermic Additions in Core Filler on Arc Stability and Microstructure during Self-Shielded, Flux-Cored Arc Welding. *Crystals* **2024**, *14*, 335. [[CrossRef](#)]
34. Park, S.; Won, J.; Yoo, S.; Moon, B.; Kim, C.; Kang, N. Influence of welding position and dilution on mechanical properties and strengthening design of flux cored arc weld metal for high manganese steels. *Int. J. Adv. Manuf. Technol.* **2024**, *130*, 3509–3523. [[CrossRef](#)]
35. Trembach, B.; Trembach, I.; Maliuha, V.; Knyazev, S.; Krbata, M.; Kabatskyi, O.; Balenko, O.; Zarichniak, Y.; Brechka, M.; Mykhailo, B.; et al. Study of self-shielded flux-cored wire with exothermic additions CuO-Al on weld bead morphology, microstructure, and mechanical properties. *Int. J. Adv. Manuf. Technol.* **2025**, *137*, 4685–4711. [[CrossRef](#)]
36. Trembach, B.; Silchenko, Y.; Balenko, O.; Hlachev, D.; Kulahin, K.; Heiko, H.; Bellorin-Herrera, O.; Khabosha, S.; Zakovorotnyi, O.; Trembach, I. Study of the hardfacing process using self-shielding flux-cored wire with an exothermic addition with a combined oxidizer of the Al-(CuO/Fe₂O₃) system. *Int. J. Adv. Manuf. Technol.* **2024**, *134*, 309–335. [[CrossRef](#)]
37. Passos, T.A.; Costa, H.; Luz, F.K.C.; Pintaude, G. The Effect of the Dilution Level on Microstructure and Wear Resistance of Fe-Cr-CV Hardfacing Coatings Deposited by PTA-P. *Coatings* **2022**, *12*, 1835. [[CrossRef](#)]
38. *DIN 1614-1:1990*; Cold-Rolled Steel Sheet and Strip; Technical Delivery Conditions; General Quality Grade (St 12 to St 34). Deutsches Institut für Normung e.V. (DIN): Berlin, Germany, 1990.
39. Guyon, I.; Elisseeff, A. An introduction to variable and feature selection. *J. Mach. Learn. Res.* **2003**, *3*, 1157–1182. [[CrossRef](#)]
40. Trembach, B.; Grin, A.; Turchanin, M.; Makarenko, N.; Markov, O.; Trembach, I. Application of Taguchi method and ANOVA analysis for optimization of process parameters and exothermic addition (CuO–Al) introduction in the core filler during self-shielded flux-cored arc welding. *Int. J. Adv. Manuf. Technol.* **2021**, *114*, 1099–1118. [[CrossRef](#)]
41. Alao, A.R.; Konneh, M. Application of Taguchi and Box-Behnken designs for surface roughness in precision grinding of silicon. *Int. J. Precis. Technol.* **2011**, *2*, 21–38. [[CrossRef](#)]
42. Matsuoka, N.; Terano, M.; Ishiguro, T.; Abe, E.; Yukawa, N.; Ishikawa, T.; Ueshima, Y.; Yamamoto, K.; Isobe, K. Computer Simulation of Deformation Behavior of Non-metallic Inclusion in Hot-rolling. *Procedia Eng.* **2014**, *81*, 120–125. [[CrossRef](#)]
43. Liu, H.; Zhang, S.; Zhang, J.; Ren, Q.; Zhang, L.; Ge, Y. Properties of typical non-metallic inclusions in steel: First-principles calculations. *Mater. Today Commun.* **2023**, *34*, 105118. [[CrossRef](#)]
44. Jafarian, H.R.; Sabzi, M.; Mousavi Anijdan, S.H.; Eivani, A.R.; Park, N. The Influence of Austenitization Temperature on Microstructural Developments, Mechanical Properties, Fracture Mode and Wear Mechanism of Hadfield High Manganese Steel. *J. Mater. Res. Technol.* **2021**, *10*, 819–831. [[CrossRef](#)]
45. Wang, J.; Li, H.; Hu, C.; Wang, Z.; Han, K.; Liu, D.; Wang, J.; Zhu, Q. The Efficiency of Thermite-Assisted Underwater Wet Flux-Cored Arc Welding Process: Electrical Dependence, Microstructural Changes, and Mechanical Properties. *Metals* **2023**, *13*, 831. [[CrossRef](#)]

Disclaimer/Publisher’s Note: The statements, opinions and data contained in all publications are solely those of the individual author(s) and contributor(s) and not of MDPI and/or the editor(s). MDPI and/or the editor(s) disclaim responsibility for any injury to people or property resulting from any ideas, methods, instructions or products referred to in the content.